NASA Contractor Report 189645

ADAPTIVE NONLINEAR POLYNOMIAL NEURAL NETWORKS FOR CONTROL OF BOUNDARY LAYER/STRUCTURAL INTERACTION

B. Eugene Parker, Jr.
Richard L Cellucci
Dean W. Abbott
Roger L. Barron
Paul R. Jordan, III

BARRON ASSOCIATES, INC
Route One, Box 159
Stanardsville, Virginia 22973-9511

and

H. Vincent Poor
Department of Electrical Engineering
Princeton University
Princeton, New Jersey 08544-5263

Contract NAS1-19271
December 1993

National Aeronautics and
Space Administration

Langley Research Center
Hampton, Virginia 23681-0001

Foreword

This Phase I Small Business Innovation Research (SBIR) final report has been prepared by Barron Associates, Inc., Stanardsville, Virginia, to document the work performed from January 16 to August 15, 1991, under Contract NAS1-19271 with the NASA Langley Research Center, Structural Acoustics Branch.

The authors express their gratitude to Drs. Richard J. Silcox, Technical Monitor, and Lucio Maestrello for their assistance in the formulation of the models utilized in this report and for their encouragement and support.

Opinions expressed in this report are those of the authors and Barron Associates, Inc., who are solely responsible for its content.

Abstract

The acoustic pressures developed in a boundary layer can interact with an aircraft panel to induce significant vibration in the panel. Such vibration is undesirable due to the aerodynamic drag and structure-borne cabin noise that result. The overall objective of this work is to develop effective and practical feedback control strategies for actively reducing this flow-induced structural vibration.

This report describes the results of initial evaluations using polynomial neural network-based feedback control to reduce flow-induced vibration in aircraft panels due to turbulent boundary layer/structural interaction. Computer simulations are used to develop and analyze feedback control strategies to reduce vibration in a beam as a first step. The key differences between this work and that ongoing elsewhere in the active control of structural vibration are, firstly, that turbulent and transitional boundary layers represent *broadband* excitation and thus present a more complex stochastic control scenario than that of narrowband (e.g., laminar boundary layer) excitation; and, secondly, that the proposed controller structures are *adaptive nonlinear infinite impulse (IIR) response polynomial neural networks*, as opposed to the traditional adaptive linear finite impulse (FIR) response filters used in most studies to date.

The controllers implemented in this study achieved vibration attenuations of 30 to 60 dB, depending on the type of boundary layer established by laminar, turbulent, and intermittent laminar-to-turbulent transitional flows. Application of multi-input, multi-output, adaptive, nonlinear feedback control of vibration in aircraft panels based on polynomial neural networks appears to be feasible today. Plans are outlined for Phase II of this study, which will include extending the theoretical investigation conducted in Phase I, and verifying the results in a series of laboratory experiments involving both beam and plate models.

Table of Contents

Figures

Tables

1 Introduction

The acoustic pressures developed in a boundary layer can interact with an aircraft panel to induce significant vibration in the panel. Such vibration is undesirable due to the aerodynamic drag and structure-borne cabin noise that result. The overall objective of the proposed work is to develop effective and practical feedback control strategies for actively reducing this flow-induced vibration of aircraft panels.

This report describes the results of initial evaluations using neural network-based feedback control strategies to reduce flow-induced vibration due to turbulent boundary layer/structural interaction. Computer simulations are used to develop and analyze feedback control strategies to reduce the vibration in a beam as a first step. There are two key differences between this work and that ongoing elsewhere in the active control of structural vibration. Firstly, that turbulent and transitional boundary layers represent *broadband* excitation and thus present a more complex stochastic control scenario than that of narrowband, deterministic excitation, such as from propeller-induced noise. Secondly, that the proposed controller structures are *adaptive nonlinear infinite impulse response (IIR) polynomial neural networks*, as opposed to the traditional adaptive linear finite impulse response (FIR) filters used in most studies to date.

Simulation involved two basic modeling tasks: modeling the *beam response* and modeling the *excitation field*. Both of these issues are discussed herein. With regard to the panel response, the basic assumption invoked is that this response can be described as *linear*, as is conventionally done in studies of panel vibration (see, e.g., [25]). Such a model can be developed from the basic principles of plate theory [5, 8], and this is the approach that is adopted here.

Due to the complexity of the flow processes of interest, useful models for the excitation field are necessarily stochastic. For self-preserving boundary layers, such as those occurring in purely turbulent flow, the excitation field can be assumed to be a Gaussian random field (e.g., [3]). Under this assumption, it is sufficient to model the excitation in terms of its second-order statistical properties, specified in terms of correlation or spectral properties of the excitation. Experimentally-derived models for the second-order structure of the turbulent boundary layer (as it interacts with the panel structure) are reported in [17-19, 24]. Certain of these models will be adopted here as the bases for the development of linear stochastic control stategies for flow-induced panel vibration due to turbulent boundary layers.

In addition to studying the control of vibration in response to a turbulent boundary layer, this initial study also focuses on the control of vibration induced by laminar-to-turbulent transitional boundary layers. Transitions from laminar to turbulent flows

result in non-equilibrium boundary layers, which cannot be modeled accurately as Gaussian random fields. In particular, the behavior of the pressure at a point in a laminar-to-transition zone region resembles an intermittently gated random signal [5, p. 579]. Even though the random signals themselves are Gaussian (i.e., they are the pressures of purely turbulent flow, or of purely laminar flow), the resultant of the intermittent gating produces a non-Gaussian signal. Modeling of this type of excitation for the purposes of vibration control can take one of two forms, depending on the control strategy to be applied. If a linear control structure is to be used, then it is sufficient to model the excitation based on its second-order statistical properties, specified in terms of the correlation or spectral properties of the excitation. Second-order models for the pressure field due to laminar-to-turbulent transition zones are described, for example, in [9] and [5, Eq. 8-71]. These models, perhaps with suitable modifications, can be used as the bases for developing linear stochastic control stategies for transitional-flow-induced panel vibration.

Optimum linear feedback control based on second-order modeling is globally optimum for the control of Gaussian vibration fields. However, the non-Gaussian excitation found in transitional boundary layers will produce a non-Gaussian vibration field in the panel to be controlled, and the corresponding optimum stochastic control strategies will therefore be nonlinear. Effective and adaptive approximations to such optimum control strategies are also likely to be nonlinear, and as such can be implemented using the general structure of nonlinear polynomial networks (e.g., [4]). Since these transition zone regions are potentially a major source of vibration in aircraft panels, it is essential that their full statistical behavior (i.e., not only their second-order characteristics) be appropriately modeled in the process of developing vibration control strategies. Even if linear control strategies based on second-order models were to emerge as being nearly as effective as fully optimal nonlinear solutions (an eventuality that is *not* clearly likely), their relative effectiveness could only be assessed through consideration of higher-order statistical characteristics of the flow.

This report is organized as follows. Section 2 describes the fundamental stochastic partial differential equations (PDEs) that model the response in the linear regime of a flat plate immersed in a fluid, when subjected to a boundary pressure field. Section 3 discusses the acoustic damping arising in such a model due to the interaction of the fluid with the plate. Two basic models are discussed in this context, corresponding to the cases of subsonic and supersonic fluid motion. Section 4 describes two experimentally-determined stochastic models, again corresponding to the subsonic and supersonic regimes, for a turbulent boundary convected over the panel. Section 5 discusses the decomposition of the panel motion into its modal behavior, and Section

6 discusses the modeling of sensor and actuator configurations. In Section 7, the overall model is described in some detail for the lower-dimensional problem of controlling a vibrating beam, and in Section 8 a hierarchical succession of benchmark examples is proposed for computer simulation of the boundary layer/structural interaction. In Section 9, experimental results are given demonstrating the effectiveness of feedback control in active vibration suppression for a beam excited by laminar and turbulent boundary layers, as well as laminar-to-turbulent transitions of the boundary layer. Finally, in Section 10, future directions for continuance of this work in Phase II are briefly outlined.

2 A Fundamental Model for Panel Response

We wish to model the motion of a thin, flat rectangular panel occupying the region $\mathcal{R} = \{0 \leq x \leq a, 0 \leq y \leq b, z = 0\}$, over which a turbulent fluid is flowing at an average velocity v in the positive x direction. It is assumed that the plate is of uniform stiffness, and is clamped at the edges.

The motion of such a plate is described by the stochastic PDE [8]

$$\left(D\nabla^4 + \rho_1 \frac{\partial^2}{\partial t^2}\right) w = f + d, \tag{2.1}$$

where w, f, and d are fields (in this case, functions of x, y, and time t) representing the plate displacement, the external pressure due to the turbulent boundary layer, and damping, respectively, all taken as being positive in the negative z direction. Here, ∇^4 is the *biharmonic operator*

$$\nabla^4 = \left(\frac{\partial^4}{\partial x^4} + 2\frac{\partial^4}{\partial x^2 \partial y^2} + \frac{\partial^4}{\partial y^4}\right); \tag{2.2}$$

D is the *plate rigidity*; and ρ_1 is the mass density (per unit area) of the panel. The plate Eq. 2.1 is subject to the boundary conditions imposed by the clamped edges:

$$w(0, y, t) \equiv w(a, y, t) \equiv w(x, 0, t) \equiv w(x, b, t) \equiv 0. \tag{2.3}$$

It is assumed that the external pressure field is due exclusively to a turbulent boundary layer on the $z > 0$ side of the plate. In this case, the forcing field f can be modeled as a homogeneous Gaussian random field whose second-order statistics will be described below.

The damping field $d(x,y,t)$ can include both structural and acoustic damping terms. Structural damping is modeled by including a term $d_s = -\gamma_s \frac{\partial}{\partial t} w$ in d, where $\gamma_s > 0$ is a coefficient of structural damping [19]. Acoustic damping is due to the feedback effects of an acoustic velocity potential, $\phi(x,y,z,t)$, launched into the fluid by the plate motion [24]. The evolution of this potential is governed by the wave equation

$$c^2 \nabla^2 \phi = \left(\frac{\partial}{\partial t} + v \frac{\partial}{\partial x} \right)^2 \phi, \quad z > 0, \tag{2.4}$$

where $\nabla^2 = \left(\frac{\partial^2}{\partial x^2} + \frac{\partial^2}{\partial y^2} + \frac{\partial^2}{\partial z^2} \right)$ is the Laplacian operator, and c is the speed of sound in the fluid. This potential is driven by the plate motion via the boundary condition:

$$\frac{\partial}{\partial z} \phi(x,y,z,t)|_{z=0} = \frac{\partial}{\partial t} w(x,y,t). \tag{2.5}$$

The resultant damping field coupled into the plate is then given by

$$d_a(x,y,t) = \rho_2 \left(\frac{\partial}{\partial t} + v \frac{\partial}{\partial x} \right) \phi(x,y,0,t), \tag{2.6}$$

where ρ_2 is the mass density of the fluid.

3 Damping Models

We will consider two specific damping models, corresponding to subsonic and supersonic flow, respectively, within the general model described above.

3.1 Subsonic Flow

For subsonic flow ($v < c$), the viscous damping can be treated as an additional term of the form $d_a = -\gamma_a \frac{\partial}{\partial t} w$ with $\gamma_a > 0$ [19]; thus the equation of interest is a second-order (in time) stochastic PDE:

$$\left(D \nabla^4 + \rho_1 \frac{\partial^2}{\partial t^2} + \gamma \frac{\partial}{\partial t} \right) w = f, \tag{3.1}$$

with $\gamma = \gamma_s + \gamma_a$. This type of damping is know as *proportionate damping*; and, although it is somewhat *ad hoc*, it has the virtues of parsimonious description and intuitive simplicity. Unfortunately, this model is too simple to accurately describe the

damping observed in physical plates. A related damping model that is more consistent with observed behavior introduces proportionate damping terms in *each mode* of the plate, allowing γ to vary with mode number [19].

In particular, with proportionate damping, we note that the behavior of a given mode (say, the m^{th}) in the eigenfuntion decomposition of the panel motion will have the dynamics of a simple mass-spring system, described by the following scalar second-order ordinary linear differential equation:

$$\left(\rho_1 \frac{d^2}{dt^2} + \gamma \frac{d}{dt} + D\lambda_m\right) w_m(t) = f_m(t). \tag{3.2}$$

The dynamics of this system are those of a damped harmonic oscillator with damping ratio $\zeta = \gamma/2\omega_m\rho_1$ and damped resonant frequency $\omega_d = \omega_m\sqrt{1-\zeta^2}$, where the undamped natural frequency ω_m equals $\sqrt{D\lambda_m/\rho_1}$. A closer fit to actual panel behavior can be achieved by allowing γ to vary with m. That is, we consider temporal modal displacements $w_m(t)$ satisfying the differential equation

$$\left(\rho_1 \frac{d^2}{dt^2} + \gamma_m \frac{d}{dt} + D\lambda_m\right) w_m(t) = f_m(t). \tag{3.3}$$

This does not translate back into the simple global proportionate damping model of Eq. 3.1 when the modes are superimposed. Rather it provides a richer damping model while preserving the linearity and analytical tractability of the eigen-decomposed plate model.

Of course, the individual modal dynamics are still those of mass-spring systems with the only modification being that the damping ratios become $\zeta_m = \gamma_m/2\omega_m\rho_1$. As with a global damping based upon γ, the individual modal damping coefficients γ_m must be chosen empirically. For example, one choice suggested in [19] for a specific class of plates is $\gamma_m \propto \omega_m^{1/3}$. Typically, the range of damping ratios ζ that one would expect in panels are on the order of 0.001 to 0.01.

3.2 Supersonic Flow

For supersonic flow ($v > c$), the modeling of the acoustic damping is more complex. In this case, the relationship between the motion of the plate and the acoustic potential at the surface of the plate is described by [25]:

$$\tilde{\phi}(x,y,0,\omega) = \int_0^b \int_0^a G(x-x',y-y',\omega)\left(-i\omega + v\frac{\partial}{\partial x'}\right)\tilde{w}(x',y',\omega)dx'dy', \tag{3.4}$$

where $\tilde{\phi}$ and $\tilde{w}$ are the Fourier transforms of ϕ and w, respectively, as functions of their time variable t; and where G is a Green's function for the system of Eqs. 2.4-2.6, given by:

$$G(x,y,\omega) = \begin{cases} -\frac{1}{\pi} exp\, \frac{iMkx}{M^2-1} \frac{cos(\frac{k}{M^2-1}\sqrt{x^2-(M^2-1)y^2})}{\sqrt{x^2-(M^2-1)y^2}} & \text{if } x > |y|\sqrt{M^2-1} \\ 0 & \text{otherwise} \end{cases}, \tag{3.5}$$

where $k = \omega/c$, and M is the Mach number ($M = v/c$).

The integral in Eq. 3.4 has a strong singularity of the Cauchy type along the intersection of the Mach cone with the $z = 0$ plane. Thus, the evaluation of this transfer characteristic requires some care.

4 Stochastic Models for the Turbulent Boundary Layer

The forcing field f in Eq. 2.1 is the pressure exerted on the plate by the turbulent boundary layer. This field can be modeled as being a homogeneous Gaussian field [15], and thus its specification requires only the determination of the second-order correlation function of the field; *viz.*:

$$\Gamma_1(\xi,\eta,\tau) \equiv \langle f(x,y,t) f^*(x+\xi, y+\eta, t+\tau) \rangle. \tag{4.1}$$

We consider two different models for this correlation structure, corresponding to experimentally-derived models for the subsonic and supersonic cases.

In the supersonic case, we consider the model [25]:

$$\Gamma_1(\xi,\eta,\tau) = \langle p^2 \rangle \sum_{n=1}^{4} \left\{ \frac{2A_n K_n e^{-|\xi|/\alpha_1\delta} e^{-|\eta|/\alpha_2\delta}}{K_n^2 + (v/\delta U_c)^2(\xi - U_c\tau)^2} \right\}, \tag{4.2}$$

where the As, Ks and αs are constants, δ is the boundary layer thickness, U_c is the convective velocity (assumed to be less than v), and $\langle p^2 \rangle$ is the mean-square intensity of the forcing field. Experimentally determined values for the A_n and K_n parameters are given by $A_1 = 4.4 \times 10^{-2}, A_2 = 7.5 \times 10^{-2}, A_3 = -9.3 \times 10^{-2}, A_4 = -2.5 \times 10^{-2}, K_1 = 5.78 \times 10^{-2}, K_2 = 2.43 \times 10^{-1}, K_3 = 1.12$, and $K_4 = 11.57$. Specific values of the remaining parameters for a benchmark example will be given below.

An empirically-determined model for the pressure field in the subsonic case is described by the covariance structure [17]:

$$\Gamma_1(\xi,\eta,\tau) = \langle p^2 \rangle \sum_{n=1}^{3} \left\{ \frac{2A'_n K'_n e^{-|\xi|/U_c\theta}}{(K'_n)^2 + (1/\delta^*)^2[(\xi - U_c\tau)^2 + \eta^2]} \right\}, \qquad (4.3)$$

where θ, the A's and K's are constants; and where δ^* denotes the boundary layer displacement thickness. Note that this is only one of several similar models that have been proposed for the pressure field of a subsonic turbulent boundary layer [17, 19], and it is chosen primarily because of its functional similarity to Eq. 4.2 in the two key variables (*viz.* ξ and τ). Experimentally determined values of A'_n and K'_n parameters are given by $A'_1 = 0.24, A'_2 = 1.08, A'_3 = 1.80, K'_1 = 0.47, K'_2 = 3.0$, and $K'_3 = 14.0$. As for the supersonic model, benchmark values of the remaining parameters will be specified below.

As noted in the Section 1, this Gaussian model for the pressure induced by the boundary layer is not suitable for transitional boundary layers. Later in this report, we implement a model of the transitional boundary layers, representing non-Gaussian excitation. To do so, we consider a model that treats the pressure field under all conditions as a mixture of those induced by purely laminar and purely turbulent flows, each of which can be modeled as a Gaussian random field. (Actually, the laminar flow can be modeled as being sinusoidal without significantly sacrificing accuracy.) The mixing of these two flows can be modeled by an independent, binary gating field, that switches intermittently between the two equilibrium boundary layers. This binary field can, in turn, be modeled as being Markovian in space and in time (i.e., it can be modeled as a dynamic Gibbs field), with transistion statistics that can be parameterized to yield either of the pure states or any degree of transition. This then, will add parameters to the model in addition to those discussed above. It should be noted that such a strategy could also be used to develop more refined second-order models, analogous to those of Eqs. 4.2 and 4.3, for the transition-zone statistics; although a full-order statistical model is of primary interest in the present context of developing algorithms for vibration control.

5 Evolution in Terms of Spatial Modes

In order to create a more parsimonious desciption of the evolution described by Eq. 2.1, it is useful to represent all spatial characteristics in terms of the modes of the plate via a set of orthonormal eigenfunctions of the biharmonic operator, ∇^4. In particular,

on denoting by $\{\lambda_k\}_{k=1}^{\infty}$ and $\{\psi_k\}_{k=1}^{\infty}$ the eigenvalues and corresponding orthonormal eigenfunctions of ∇^4 (i.e., solutions to $\nabla^4\psi = \lambda\psi$), we can then write Eq. 2.1 as the vector differential equation:

$$\left(\rho_1 \frac{d^2}{dt^2} + \gamma_v \frac{d}{dt} + D\Lambda\right) \underline{w}(t) = \underline{f}(t) + \underline{a}(t), \tag{5.1}$$

where, Λ is the diagonal matrix with diagonal elements $\lambda_1, \lambda_2, \ldots$; and for each $k = 1, 2, \ldots$, the k^{th} components of $\underline{w}(t)$, $\underline{f}(t)$, and $\underline{c}(t)$ are given by

$$w_k(t) = \int_0^b \int_0^a w(x,y,t)\psi_k(x,y)dxdy, \tag{5.2}$$

$$f_k(t) = \int_0^b \int_0^a f(x,y,t)\psi_k(x,y)dxdy, \tag{5.3}$$

and

$$a_k(t) = \int_0^b \int_0^a d_a(x,y,t)\psi_k(x,y)dxdy. \tag{5.4}$$

(Of course $a_k(t)$ is simply $-\gamma_a \frac{d}{dt} c_k(t)$ in the subsonic case.) The displacement field at each time t is then given by the expansion

$$w(x,y,t) = \sum_{k=1}^{\infty} w_k(t)\psi_k(x,y), \quad (x,y) \in \mathcal{R}. \tag{5.5}$$

Further discussion of this expansion, including remarks on the structure of the input and damping terms, is included below.

6 Sensor and Actuator Modeling

In order to study the control of the field w we can consider three models of interest. In the first of these models, we assume that the field can be sensed throughout the region $\mathcal{R}$, and that we can apply controls at all points in $\mathcal{R}$. That is, we assume measurements of the form

$$r(x,y,t) = w(x,y,t) + n(x,y,t), \quad (x,y) \in \mathcal{R}, \quad t \geq 0, \tag{6.1}$$

where n represents a white Gaussian measurement noise field; and a control input to Eq. 2.1 of the form

$$c(x,y,t) = \int_0^t \int_0^b \int_0^a h(x,y,t;x',y',t')r(x',y',t')dx'dy'dt', \tag{6.2}$$

where h is the transfer function of the controller. Note that, in assuming a linear control law, there is no loss in generality with a quadratic loss performance criterion (e.g., minimizing squared error) since the field to be controlled is Gaussian and the measurements are linear.

This model can be decomposed into modal components. In particular, we can consider the equivalent model:

$$\underline{r}(t) = \underline{w}(t) + \underline{n}(t), \tag{6.3}$$

where $\underline{n}$ represents a vector of independent and identically distributed Gaussian white-noise processes. Within this representation, the control signal becomes

$$\underline{c}(t) = \int_0^t \mathbf{H}(t,t')\underline{r}(t')dt', \tag{6.4}$$

where the matrix function $\mathbf{H}$ has $k-l^{th}$ element

$$H_{k,l}(t,t') = \int_0^b \int_0^a \int_0^b \int_0^a h(x,y,t;x',y',t')\psi_k(x',y')\psi_l(x,y)dx'dy'dxdy. \tag{6.5}$$

This first model is primarily of theoretical interest since it is not practical to apply sensing and actuating materials to the entire panel. However, consideration of this model can provide useful insight into the controllability properties of the overall system describing the plate motion.

As a second, more realistic measurement model, we can consider the sensing/actuation of the field by point sensors/actuators placed on a lattice of points, $\{x_i, y_j; \quad i = 1,\ldots,n, j = 1,\ldots,m\}$ in $\mathcal{R}$. In the simplest case of this model, we can assume measurements of the form

$$r(x_i,y_j,t) = w(x_i,y_j,t) + N_{i,j}(t), \quad i = 1,\ldots,n, \quad j = 1,\ldots,m, \tag{6.6}$$

where $\{N_{i,j}(t), \quad i = 1,\ldots,n, \quad j = 1,\ldots,m\}$ is a family of independent and identically distributed white-noise processes. This model can be modified to include the dynamics of the sensors by replacing the terms $w(x_i,y_j,t)$ with filtered versions $w'(x_i,y_j,t)$ given by

$$\frac{d}{dt}w'(x_i,y_j,t) = -f_s w'(x_i,y_j,t) + w(x_i,y_j,t), \tag{6.7}$$

where $f_s > 0$ determines the bandwidth of the sensors. (Obviously, this model assumes identical, first-order sensors.) In terms of the modal response, the model of Eq. 6.6 can be written as

$$r(x_i, y_j, t) = \sum_{k=0}^{\infty} w_k(t)\psi_k(x_i, y_j) + N_{i,j}(t), \quad i = 1, \ldots, n, j = 1, \ldots, m; \quad (6.8)$$

or to incorporate sensor dynamics, we can replace the w_ks with w'_ks generated by

$$\frac{d}{dt}w'_k(t) = -f_s w'_k(t) + w_k(t). \quad (6.9)$$

Note that, within this model, we have multiple independent measurements of each component of $\underline{r}(t)$, but that these measurements are not independent from component to component. Of course, as the lattice becomes denser, these various measurements can be combined to provide approximately independent measurements of the components by approximating the continuous model of Eq. 6.3.

In the point-actuator model, the control signal will take the form

$$c(x, y, t) = \sum_{i=1}^{n}\sum_{j=1}^{m} c(x_i, y_j, t)\delta(x - x_i)\delta(y - y_j), \quad (x, y) \in \mathcal{R}, t \geq 0, \quad (6.10)$$

where δ denotes the Dirac delta function, and where the coefficients $c(x_i, y_j, t)$ are obtained via linear transformation of the measurements for times up to time t; that is,

$$c(x_i, y_j, t) = \sum_{i'=1}^{n}\sum_{j'=1}^{m}\int_0^t h(x_i, y_j, t; x_{i'}, y_{j'}, t')dt', \quad (6.11)$$

where the coefficent function h determines the controller. In terms of modal response, the vector control signal analogous to that of Eq. 6.4 has k^{th} component in this case given by

$$c_k(t) = \sum_{i=1}^{n}\sum_{j=1}^{m} c(x_i, y_j, t)\psi_k(x_i, y_j). \quad (6.12)$$

Analogously to Eq. 6.7, actuator dynamics can be included in this model by replacing the signals $c(x_i, y_j, t)$ with filtered versions $c'(x_i, y_j, t)$

$$\frac{d}{dt}c'(x_i, y_j, t) = -f_a c'(x_i, y_j, t) + c(x_i, y_j, t), \quad (6.13)$$

where $f_a > 0$ controls the actuator bandwidth. Of course, both Eqs. 6.7 and 6.13 can be incorporated into the plant when designing and evaluating specific control laws. As a final comment on this model, we note that this model is easily modified to allow for sensing and actuating on different lattices.

The third model of interest is that in which the sensors and actuators are placed on lattice points as above, but they are modeled as having significant dimensions. In this case we can think of an observation for each lattice point that integrates the displacement field over the subset of the panel occupied by the sensor at that lattice point. That is, on denoting the region occupied by the $i-j^{th}$ sensor by $\mathcal{R}_{i,j}$, we can integrate the continuous model of (6.1) to yield the discrete model

$$R_{i,j}(t) = W_{i,j}(t) + N_{i,j}(t). \quad i = 1, \ldots, n, j = 1, \ldots, m. \tag{6.14}$$

where $R_{i,j}(t)$, $W_{i,j}(t)$, and $N_{i,j}(t)$ denote the integrals of the fields $r(x,y,t)$, $w(x,y,t)$, and $n(x,y,t)$, respectively, from Eq. 6.1, over the region $\mathcal{R}_{i,j}$. Note that we retain the notation of Eq. 6.6 for the noise, since the noise elements $N_{i,j}(t)$ obtained by integrating $n(x,y,t)$ over the regions $\mathcal{R}_{i,j}$ form a matrix of independent white noises as was the noise model in Eq. 6.6. These noises will be identically distributed if all sensors have the same area. (It is assumed, of course, that the sensors do not overlap one another.)

The $i-j^{th}$ actuator can be assumed to apply uniform pressure over the region $\mathcal{R}_{i,j}$. Thus, the control signal in this model takes the form

$$c(x,y,t) = \sum_{i=1}^{n}\sum_{j=1}^{m} C_{i,j}(t) I_{\mathcal{R}_{i,j}}(x,y), \quad (x,y) \in \mathcal{R}, t \geq 0. \tag{6.15}$$

where $I_{\mathcal{R}_{i,j}}$ denotes the indicator function of $\mathcal{R}_{i,j}$; and where the functions $C_{i,j}(t)$ are obtained by linear transformations of the measurements Eq. 6.14 in a manner analogous to Eq. 6.11.

In modal form, the sensor model Eq. 6.14 is

$$R_{i,j}(t) = \sum_{k=0}^{\infty} w_k(t)\Psi_k(i,j) + N_{i,j}(t), \quad i = 1, \ldots, n, j = 1, \ldots, m, \quad (6.16),$$

with $\Psi_k(i,j) = \int_{\mathcal{R}_{i,j}} \psi_k(x,y)dxdy$; and the k^{th} component of the modal control signal becomes

$$c_k(t) = \sum_{i=1}^{n}\sum_{j=1}^{m} C_{i,j}(t)\Psi_k(i,j). \tag{6.17}$$

As in the point sensor/actuator model, the sensor and actuator dynamics can be introduced by replacing the quantities $W_{i,j}(t), C_{i,j}(t)$, and $w_k(t)$ with appropriately filtered versions. Also, as above, the model is easily modified to provide for non-colocated sensors and actuators.

For the Phase I analysis of the vibration control problem, it will be assumed that sensing and actuation are performed in a continuously distributed fashion. The modal controllers will assume complete knowledge of modal displacements (i.e., ideal sensing) and the ability to effect unimodal actuation (i.e., ideal actuation). Consideration of this model can provide useful insight into the controllability properties of the overall system describing the plate motion. This is appropriate for the Phase I study of the viability of active control.

We end this section with a few comments. First, note that any of the three sensing models can be combined with any of the three actuation models by a straightforward modification of the equation describing the transfer from measurements to controls. Secondly, it should be kept in mind that in a practical system, these transfer characteristics will take on a constrained form. (For example, their time behavior will likely be constrained to be that described by time-invariant, lump-parameter systems.) Thirdly, in the event that the forcing and damping functions can be modeled as autoregressive, moving-average (ARMA) processes, the *optimum* stochastic controller will take the form of an optimum state estimator (e.g., a Kalman filter), followed by an optimum deterministic controller. Finally, we recall that the assumption of linearity in the control law will not be reasonable for the generalizations of this problem in which the forcing function is a transitional field [5, 11]. This is because such fields are not Gaussian, and therefore do not yield linear structures as optimal controllers even under quadratic loss. Thus, in the case of transitional boundary layers, nonlinear mappings (such as polynomial networks) from the sensors to the actuators will replace the linear mappings of Eqs. 6.2, 6.11, etc.

7 Consideration of a Vibrating Beam

One difficulty with the panel model described in the preceding sections is that it is quite complex spatially. In order to reduce this complexity, it is useful to consider first a $y = 0$ "slice" of the problem. This simplification will still allow us to investigate many of the basic phenomena of interest, provided that the slice is oriented in the direction of fluid flow (i.e., in the x direction). Thus, we will consider the control of

the analogous stochastic PDE in two spatial dimensions (x and z):

$$\left(D\frac{\partial^4}{\partial x_4} + \rho_1\frac{\partial^2}{\partial t^2} + \gamma_s\frac{\partial}{\partial t}\right) w = f + d_a + c, \quad 0 < x < a, \quad t \geq 0, \tag{7.1}$$

where the displacement w, forcing field f, acoustic damping d_a, and feedback control c are functions of x and t. The boundary conditions are

$$w(0,t) \equiv w(a,t) \equiv 0. \tag{7.2}$$

In the supersonic case, we will consider the acoustic damping to result from an acoustic potential $\phi(x,y,t)$ evolving in the $x-z$ plane via the two-dimensional version of Eqs. 2.4-2.6:

$$c^2\left(\frac{\partial^2}{\partial x^2} + \frac{\partial^2}{\partial z^2}\right)\phi = \left(\frac{\partial}{\partial t} + v\frac{\partial}{\partial x}\right)^2\phi, \quad z > 0; \tag{7.3}$$

$$\frac{\partial}{\partial z}\phi(x,z,t)|_{z=0} = \frac{\partial}{\partial t}w(x,t); \tag{7.4}$$

and

$$d_a(x,t) = \rho_2\left(\frac{\partial}{\partial t} + v\frac{\partial}{\partial x}\right)\phi(x,0,t). \tag{7.5}$$

The spatial eigenvalues and orthonormal eigenfuctions of Eq. 7.1 are given by (e.g., [25])

$$\lambda_k = \left(\frac{\beta_k}{a}\right)^4, \tag{7.6}$$

and

$$\psi_k(x) = \frac{1}{\sqrt{a}}\left[\epsilon_k\left(sin\,\frac{\beta_k x}{a} - sinh\,\frac{\beta_k x}{a}\right) + \left(cos\,\frac{\beta_k x}{a} - cosh\,\frac{\beta_k x}{a}\right)\right], \tag{7.7}$$

where $\epsilon_k = \frac{sin\,\beta_k + sinh\,\beta_k}{cos\,\beta_k - cosh\,\beta_k}$; and $\beta_1, \beta_2, \ldots,$ are the roots of the equation $cos\,\beta\,cosh\,\beta = 1$. These roots are given approximately by $\beta_1 \doteq 4.730, \beta_2 \doteq 7.853$, and $\beta_k \doteq \pi(2k+1)/2$, for $k > 2$.

Knowledge of the eigenstructure of the clamped beam allows us to model the forcing function in the modal decomposition of Eq. 7.1. In particular, the forcing function can be written as

$$f(x,t) = \sum_{k=1}^{\infty} f_k(t)\psi_k(x), \tag{7.8}$$

with

$$f_k(t) = \int_0^a f(x,t)\psi_k(x)dx, \quad k = 1, 2, \ldots. \tag{7.9}$$

Since f is a Gaussian field, the vector process $\underline{f}(t)$ will also be Gaussian. Thus, we can model its statistics by determining its autocorrelation matrix $\mathbf{\Gamma}(\tau)$, whose $k-l^{th}$ element is given by:

$$\Gamma_{k,l}(\tau) = \langle f_k(t) f_l^*(t+\tau)\rangle = \int_0^a \psi_k(x) \int_0^a \psi_l(x')\Gamma(x-x',0,\tau)dxdx'. \tag{7.10}$$

where $\mathbf{\Gamma}$ is derived from Eq. 4.2 or 4.3, depending on whether we are considering the subsonic or supersonic case. In either case, the computation in Eq. 7.10 is simplified by first transforming to the temporal frequency domain. After Fourier transformation (in the τ variable), both Eqs. 4.2 and 4.3 reduce to the form:

$$\tilde{\Gamma}_1(\xi, 0, \omega) = F(\omega)e^{-g|\xi| + i\omega\xi/U_c}, \tag{7.11}$$

where F is a weighted sum of exponentials; and where $g = \frac{1}{U_c\theta}$ in the subsonic case, and $g = \frac{1}{\alpha_1 \xi}$ in the supersonic case. Thus, in the temporal frequency domain the elements of $\tilde{\mathbf{\Gamma}}$ are given by:

$$\tilde{\Gamma}_{k,l}(\omega) = F(\omega) \int_0^a \psi_k(x) \left[e^{-A^* x} \int_0^x \psi_l(x') e^{A^* x'} dx' + e^{Ax} \int_x^a \psi_l(x') e^{-Ax'} dx' \right] dx, \tag{7.12}$$

with $A = g + i\omega/U_c$. By inserting Eq. 7.7 into Eq. 7.12, the forcing statistics can be determined in closed form. In particular, we have

$$\tilde{\Gamma}_{k,l}(\omega) = F(\omega)[\Delta_{k,l}(\omega) + \Delta_{l,k}^*(\omega) + \Xi_{k,l}(\omega) + \Xi_{l,k}^*(\omega)], \tag{7.13}$$

where

$$\Delta_{k,l}(\omega) = \frac{[e^{-Aa}(A\psi_l^{(2)}(0) - \psi_l^{(3)}(0)) - (A\psi_l^{(2)}(a) - \psi_l^{(3)}(a))](A\psi_k^{(2)}(a) + \psi_k^{(3)}(a))}{(A^4 - \lambda_k)(A^4 - \lambda_l)}; \tag{7.14}$$

and

$$\Xi_{k,l}(\omega) = \frac{A^3\delta_{k,l} + A^2\Psi_{k,l}^{(1)} + A\Psi_{k,l}^{(2)} + \Psi_{k,l}^{(3)}}{A^4 - \lambda_k}. \tag{7.15}$$

Here, $\delta_{k,l}$ denotes the Kronecker delta; and the constants $\Psi_{k,l}^{(n)}$ are given by

$$\Psi_{k,l}^{(n)} = \int_0^a \psi_k^{(n)}(x)\psi_l(x)dx, \quad n = 1, 2, 3, \tag{7.16}$$

where here and in Eq. 7.14 $\psi_k^{(n)}(x) = d^n\psi_k(x)/dx^n$.

Note that the terms described in Eqs. 7.14 and 7.15 consist of rational functions of the frequency ω combined with pure delays. Thus, this stucture is straightforward to realize in hardware or software using linear, lumped-parameter networks with delays. Note that there are only two fixed delays, $e^{i\omega/U_c}$ and $e^{-i\omega/U_c}$, independent of the choice of k and l, so that the entire stucture $[\Delta_{k,l}(\omega) + \Delta^*_{l,k}(\omega) + \Xi_{k,l}(\omega) + \Xi^*_{l,k}(\omega)]$ can be realized as four seperate (rational) matrix networks combined with scalar time delays. The remaining part of $\tilde{\Gamma}(\omega)$ is the term $F(\omega)$, which is not rational. In particular, for the subsonic case, F is given by:

$$F(\omega) = \langle p^2 \rangle \frac{\delta^*}{v} \sum_{n=1}^{3} A'_n e^{-K'_n|\omega|\delta^*/v}; \tag{7.17}$$

and for the supersonic case, F is given by:

$$F(\omega) = \langle p^2 \rangle \frac{\delta}{U_c} \sum_{n=1}^{4} A_n e^{-K_n|\omega|\delta/U_c}. \tag{7.18}$$

Since this component of the spectrum is nonrational, it cannot be synthesized using a linear, lumped-parameter model. Fortunately, this part of the spectrum is not tied to the spatial structure; therefore, it can be synthesized as a scalar random process, which can then be fed into the spatial structure via the rational network derived from the remaining terms. The sums in Eqs. 7.17 and 7.18 can be realized by producing independent processes having the individual spectra of the summands, and then adding them together. Thus, the key to simulation of the nonrational part of this excitation is to synthesize stationary random sequences with the generic spectral shape

$$\phi(\omega) = \pi\alpha e^{-\alpha|\omega|}. \tag{7.19}$$

To consider the generation of this process in discrete time, we first note that the autocorrelation function corresponding to Eq. 7.19 is given by

$$\rho(\tau) = \frac{1}{1 + (\tau/\alpha)^2}, \quad -\infty < \tau < \infty. \tag{7.20}$$

When sampled at time instants spaced Δ time units apart, the resulting discrete-time process $\{X_k\}$ will have autocorrelation sequence

$$\rho_\Delta(k) = \langle X_t X_{t+k} \rangle = \frac{1}{1 + (k/\alpha_\Delta)^2}, \tag{7.21}$$

where $\alpha_\Delta = \alpha/\Delta$, which has the corresponding spectrum

$$\phi_\Delta(\omega) = \sum_{n=-\infty}^{\infty} \frac{e^{in\omega}}{1+(k/\alpha_\Delta)^2} = \pi\alpha_\Delta \frac{\cosh \alpha_\Delta(\pi-\omega)}{\sinh \alpha_\Delta \omega} - 1, \quad 0 \le \omega \le 2\pi. \tag{7.22}$$

Such a process can be produced by filtering a white Gaussian sequence with a linear filter having gain $\sqrt{\phi_\Delta(\omega)}$. If causality is not required, this can be accomplished simply by using the filter with transfer function $\sqrt{\phi_\Delta(\omega)}$. If, on the other hand, causality is desired, then it is necessary to factor ϕ_Δ into its causal and anti-causal spectral factors, ϕ_Δ^+ and ϕ_Δ^-, respectively, a task that must be performed numerically.

8 Benchmark Examples

In order to study the control problem in the above models, it is useful to specify benchmark values for the various parameters arising in the preceding sections.

For the subsonic case, we can choose among several scenarios studied in [19]. We assume the same panel parameters as in the supersonic case, and fix the following parameters for the boundary layer [19] (see Eq. 4.3): $v = 110m/s$, $\delta^* = 0.39cm$, $U_c = 0.8v$, and $\theta = 17\delta^*/U_c$. Again, we choose negligible damping (as in [19]) although this might perhaps be changed to a more realistic value. Within these benchmarks, we can consider the hierarchy of models listed in Table 8.1. The shaded region represents those models investigated in this Phase I report.

In studying the beam, we will take intensive quantities to have the same numerical values as their higher-dimensional counterparts in the benchmark model. Note that the above hierarchy includes non-Gaussian excitation fields (such as found in a transitional boundary layer) as described in preceding sections. This hierarchy may also be extended to include nonlinear dynamics of the beam and panel by replacing the linear equations with appropriate nonlinear modifications (see, e.g., [7]). Consideration of the models in this order allows us to study the most basic phenomena first. In the simplest case, the primary phenomenon being studied is that of a second-order, linear stochastic differential equation, driven by a nonrational (scalar) random process with the model Eq. 4.3. By performing the analysis on a modal basis, we will see the effects of the temporal spectral shape on the control problem without complications due to spatial complexity.

The latter will arise in the multimodal version of this same problem, and the complexity can be built up by adding modes until sufficiently rich modal structure is ob-

Table 8.1 Hierarchy of Models; Shaded Region Represents Those Models Investigated Experimentally in this Report

Beam	Subsonic	Gaussian	Single-Mode
			Multi-Mode
		Non-Gaussian	Single-Mode
			Multi-Mode
	Supersonic	Gaussian	Single-Mode
			Multi-Mode
		Non-Gaussian	Single-Mode
			Multi-Mode
Plate	Subsonic	Gaussian	Single-Mode
			Multi-Mode
		Non-Gaussian	Single-Mode
			Multi-Mode
	Supersonic	Gaussian	Single-Mode
			Multi-Mode
		Non-Gaussian	Single-Mode
			Multi-Mode

tained. Consideration of the supersonic case within the beam model will require the development of a Green's function for the two-dimensional acoustic potential of Eqs. 7.3-7.5 (analogous to that of Eq. 3.5). Work related to this problem can be found in [9]. Finding this Green's function is an intermediate task to finding a suitable representation for the acoustic damping in terms of the modal response of the beam. The study of the plate is a conceptually straightforward extension of the study of the beam. However, it is anticipated that the additional complexity will provide several challenges in implementing this extension. One important issue is the eigenfunction decomposition of the plate motion, which in the case of proportional damping must be accomplished by either numerical approximation, asymptotic expansion, or some other approximation method. One promising such method is that applied in [25], in which the modal behavior is approximated by separating the modal structure into one-dimensional (x and y) components. For non-proportional damping, eigenfunction decomposition is not possible. These are issues to be addressed in the follow-on to the current study.

9 Experimental Results

In this section we describe the results of computer simulation experiments that were conducted on a clamped beam as a first step toward adaptive nonlinear feedback

controls for reducing the vibratory response of aircraft panels subjected to a turbulent boundary layer. Investigation is limited to the shaded region in Table 8.1.

9.1 Control System Simulation

We consider in this section the details of experiments at the first level in the hierarchy described in the preceding section. That is, we consider the control of the fundamental mode of a clamped beam subjected to a subsonic flow.

A system model for this problem is the following forced, undamped scalar second-order ordinary linear differential equation (see Eq. 5.1):

$$\left(\rho_1 \frac{d^2}{dt^2} + \gamma \frac{d}{dt} + D\lambda_1\right) w_1(t) = f_1(t) + c_1(t), \tag{9.1}$$

where ρ_1 and D are the density and rigidity, respectively, of the beam; λ_1 is the principal eigenvalue of the biharmonic operator in one dimension (i.e., Eq. 7.6 with $k = 1$); and where w_1, f_1, and c_1 denote the projections of the beam displacement, forcing field, and control applied, respectively, onto the principal spatial eigenfunction, ψ_1, of the beam. Unless otherwise specified, $\gamma_m = 0.5\ \omega_d^{1/3}$, where $\omega_d = \omega_m \sqrt{1 - \zeta_m^2}$ is the damped natural frequency of mode m, ω_m is the undamped natural frequency of mode m, and ζ_m is the damping ratio; these terms were discussed in Section 3, and are discussed further in Appendix A and B.

Note that the homogeneous version of Eq. 9.1 is a damped oscillator with resonant frequency

$$\nu_1 = \frac{\sqrt{D\lambda_1 / \rho_1}}{2\pi} . \tag{9.2}$$

For the benchmark parameter values set forth in the above section, the principal eigenvalue is

$$\lambda_1 = \left(\frac{\beta_1}{a}\right)^4 \tag{9.3}$$

and thus the resonant frequency of Eq. 9.1 is

$$\nu_1 = 90.86\ Hz. \tag{9.4}$$

The resonant frequencies are tabulated in Table 9.1 for the different modes.

Table 9.1: First Ten Eigenvalues and Corresponding Natural Temporal Frequencies of Benchmark Beam

Mode Number (m)	λ_m ($\times 10^4$)	f_m(Hz)	ω_m(rad/sec)
1	5.7842	90.862	570.90
2	43.948	250.46	1,573.6
3	168.92	491.02	3,085.1
4	461.58	811.68	5,099.9
5	1,030.0	1,212.5	7,618.3
6	2,009.3	1,693.5	10,640
7	3,561.6	2,254.7	14,166
8	5,875.9	2,896.0	18,196
9	9,168.4	3,617.5	22,729
10	13,682	4,419.1	27,766

To design an experiment for assessing the effectiveness of adaptive control according to Eq. 9.1, we first convert this model to discrete time. As will be seen, a sampling rate f_S of 10,000 samples per second (i.e., a sampling interval of 100 μsec.) will provide ample margin for implementing a digital control on Eq. 9.1; this is the sampling rate used in the simulations. On defining the sampled displacement and input sequences as

$$w_k = w_1(k\,\Delta), \qquad k = 0, 1, \ldots \tag{9.5}$$

and

$$f_k = f_1(k\,\Delta), \qquad k = 0, 1, \ldots \tag{9.6}$$

where $\Delta = 1/f_S$, and k is now the time index, we can write a discrete-time plant model corresponding to Eq. 9.1 as (see Appendix A for derivation)

$$\begin{bmatrix} w_{k+1} \\ \dot{w}_{k+1} \end{bmatrix} = \begin{bmatrix} e^{-\alpha\Delta}[\gamma \sin(\omega_d\Delta)/\rho_1 - \alpha \sin(\omega_d\Delta) + \omega_d \cos(\omega_d\Delta)]/\omega_d & e^{-\alpha\Delta}\sin(\omega_d\Delta)/\omega_d \\ -\omega_m^2\, e^{-\alpha\Delta}\sin(\omega_d\Delta)/\omega_d & e^{-\alpha\Delta}[\cos(\omega_d\Delta) - \alpha \sin(\omega_d\Delta)/\omega_d] \end{bmatrix}$$

$$\begin{bmatrix} w_k \\ \dot{w}_k \end{bmatrix} + \begin{bmatrix} 0 \\ \Delta/\rho_1 \end{bmatrix} f_k + \begin{bmatrix} 0 \\ \Delta/\rho_1 \end{bmatrix} c_k \tag{9.7}$$

for $k = 0, 1, \ldots$, where $\dot{w}_k$ is the state variable representing the time derivative of $w_k(t)$ at the sampling times $t = k\Delta$.

For the purposes of experimentation, we assume that we can observe directly the motion of the beam projected onto the fundamental modes (i.e., ideal sensing). The case of practical, discrete sensors is discussed further in Section 11.3. We also assume that we can measure the sequence $w_1, w_2, \ldots$, without error (i.e., the noiseless case). The situation in which there is measurement error is a straightforward modification of this case. Moreover, we assume that we can apply a control c_k at each sample time k. For a stochastic plant such as Eq. 9.7, the control sequence $\{c_k\}$ must, of course, be a function of the system outputs; i.e., for each k, c_k will depend on previous w_ks.

Fig. 9.1 illustrates a block diagram of the complete simulated system with unity feedback control for each vibration mode; note that each mode to be controlled has a similar control loop. Simulation of the dynamics is direct from the plant and controller equations. The reference input is taken to be zero since this is the desired amount of modal deflection. The sequence $\{w_m(t)\}$, the modal displacement of the m^{th} mode, is thus a direct measure of the error signal. The error signal drives the controller, which synthesizes a modal actuation, $c_m(t)$, that is summed with the turbulent modal force, $f_m(t)$, that together drive the plant (i.e., act on the beam). The action taken by the controller should be such that the modal displacement, $w_m(t)$, remains close to the reference input, which is taken to be zero.

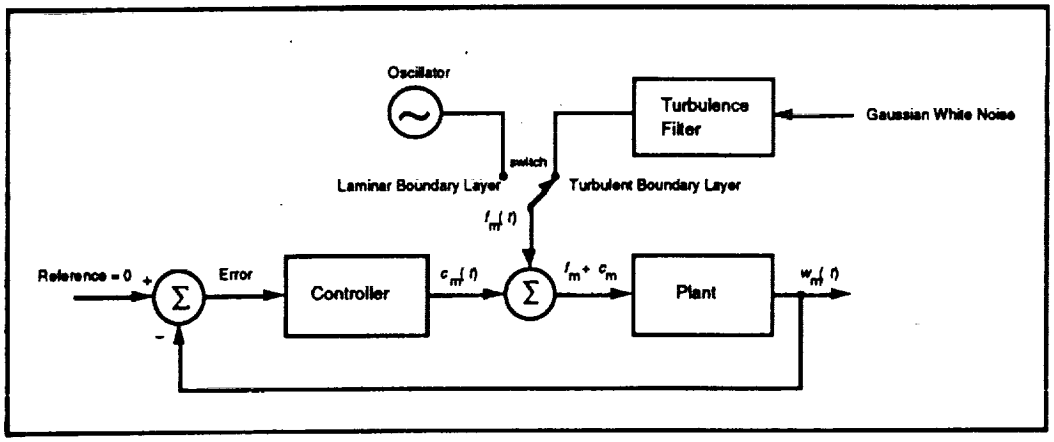

Figure 9.1: Block Diagram of Control System for Modal Response of Beam

$$<\frac{1}{m}\sum_{k=1}^{m} w_k^2> \tag{9.8}$$

Assuming as an objective the minimization of the average vibrational energy over m modes, an optimal control strategy can be specified for this problem; note that <·> denotes the *expected value* of the bracketed quantity. Generally, since $F(\omega)$ is not rational but instead exponential, this control will be produced by an infinite impulse response (IIR) filtration of the measurement sequence. An IIR filter structure has particular advantages for the problem of interest here, in that it is easily adapted; it is also easily generalized for the nonlinear case in which the linear predictor is replaced with a nonlinear polynomial neural network predictor.

If the forcing input were a rational process, then the optimum filter would have a recursive implementation as a Kalman state predictor. However, for the case at hand, the system is not rational, and the optimal controller will not, in general, have such a simple implementation. As discussed below, however, since the forcing function is being modeled as an ARMA process, the optimum stochastic controller will take the form of an optimum state estimator (e.g., a Kalman filter).

In its adaptive form, the objective of minimizing Eq. 9.8 is replaced with that of minimizing the raw squared average:

$$\frac{1}{m}\sum_{k=1}^{m} w_k^2. \tag{9.9}$$

The basic design issue is that of creating an adaptation algorithm to minimize the objective of Eq. 9.9 within the dynamical model (i.e., Eq. 9.7). The spatial issues have been removed by the projection of the spatial structure onto the principal eigenspace of the biharmonic operator. In this way, we reduce the problem to the above-described scalar problem in which we have the scalar measurement sequence $\{w_t\}$. Note that, in a real system, an approximation to such a measurement can be produced by combining the outputs of an array of sensors distributed on the beam. The outputs of these sensors can be combined at each sampling time in a way that mimics the projection of the displacement onto the eigenfuntion ψ_m:

$$w_m(t) = \int_0^a \psi_m(x)\, w(x,t)\, dx. \tag{9.10}$$

Note that from the viewpoint of the controller, the plant is unknown. This makes developing a controller difficult, since to determine its coefficients, one would ideally know the *desired* output of the controller in real time. The first approach that was attempted in designing a controller was to try to predict $f_m(t)$ based on knowledge of both the plant and the previous measurements of $\{w_k\}$, with the intention of setting $\hat{c}_m(t) = -f_m(t)$, where $\hat{c}_m(t)$ represents an *estimate* of $c_m(t)$; the sequence of previous measurements $\{w_k\}$ must be used instead of $\{f_k\}$ since the latter is not available. In designing such a controller one obtains for each mode an equation of the form

$$\frac{1}{n}\sum_{t=1}^{n} w_t^2 = \frac{1}{n}\sum_{t=1}^{n} [f_t - \hat{f}_{t|t-2} + 2(f_{t-1} - \hat{f}_{t-1|t-2})]^2 , \tag{9.11}$$

where $\{w_t\}$ is the modal beam displacement, $\{f_t\}$ is the modal forcing signal (i.e., boundary-layer pressure), and $\hat{f}_{t|t-2}$ and $\hat{f}_{t-1|t-2}$ are optimum two-step-ahead and one-step-ahead predictors of $\{f_t\}$, respectively.

When an FIR transversal filter based on this approach was implemented, it was found to be highly unstable; any error in predicting $\{f_t\}$ introduced an error in the control signal input to the plant; this in turn increased the modal displacement error, which then had to be compensated for along with the turbulence force at the next time step.

An alternative strategy was then implemented which proved to be highly successful. It is based on the notion of making *no* assumptions regarding the temporal relationship between $c_m(t)$ and $f_m(t)$. The controller is implemented as an IIR filter using a separate dynamic polynomial network nodal element, as shown in Fig. 9.2, to control the displacement in each mode. Note that an IIR filter was used instead of an FIR filter since it was expected to reduce the number of terms necessary in the control system.

When designing an estimation neural network for the purpose of smoothing, filtering, or prediction, the structure of the network can be established using the Barron Associates, Inc. (BAI) *Algorithm for Synthesis of Polynomial Networks (ASPN-II)* [13]. This software package is used to structure and parameterize static (i.e., FIR) networks; similar algorithms exist for structuring and parameterizing dynamic (i.e., IIR) polynomial networks [1]. However, because the modal displacement error input to the controller is a function of previous control outputs, such algorithms cannot be used to structure and parameterize the controller *a priori;*

instead, *the proper controller must be identified during the process of controlling.* In practice, BAI has found that high-order controllers are generally not necessary. Accordingly, a simple dynamic nodal element feeding back the two previous control outputs, $\hat{c}_m(t-1)$ and $\hat{c}_m(t-2)$, and the three previous measurement values, $w_m(t-1)$ and $w_m(t-2)$, was attempted initially. Because this structure performed well, attempt was made to reduce the number of measurement value feedback terms. It was found that the minimum adequate controller is one that feeds back the two previous control outputs and the two previous sensor measurements. No attempt was made to reduce the number of previous control outputs that are fed back: two are the minimum necessary for constructing an oscillator which, in the case of no damping, captures the basic behavior of the plant.

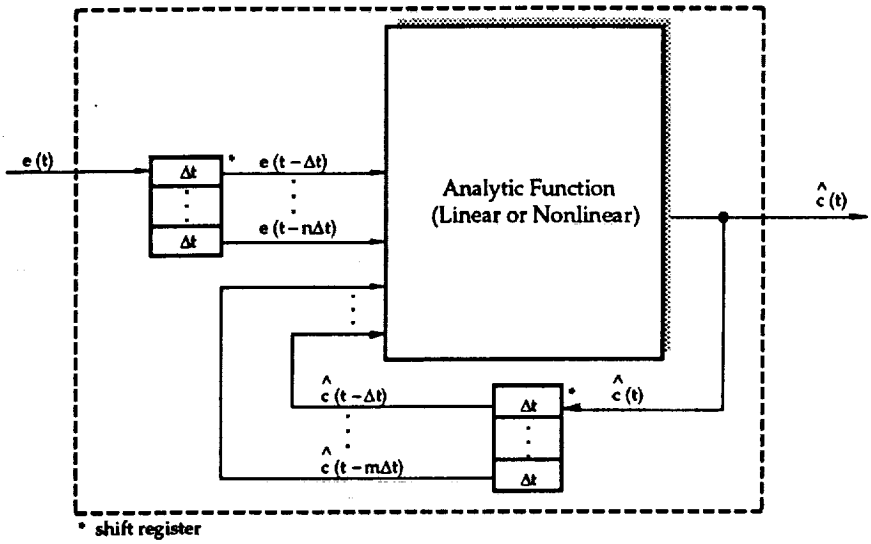

Figure 9.2: Dynamic Polynomial Neural Network Nodal Element; e(t) Represents the Modal Displacement Error and $\hat{c}(t)$ the Controller Output

In all experiments, this simple controller was trained off-line using Gaussian white noise (GWN) as the input process $f(t)$. GWN simulates any (broadband) continuous input disturbance to an arbitrary degree of accuracy. This implies that, for a plant with a given eigenstructure, in a mean-squared-error sense and without *a priori* knowledge of the temporal excitation function (other than its continuous as opposed to discrete nature), there is a single ideal control function. The spatial forcing function is

already taken into consideration in the modal response function as defined in Eq. 7.8. With this approach, the temporal excitation signal simulates any and all continuous flow conditions and thereby, indirectly, any and all boundary-layer excitations.

With all parameters initially set to zero, the simulated beam was exposed to 0.25 sec. of GWN, and the modal deflection was noted. The controller parameters were then adapted using a Guided Random Search (GRS) technique; the process is functionally similar to using the Least Mean Squares (LMS) procedure, but has been found to converge much more rapidly than the LMS algorithm. The simulated beam was then exposed to additional independent GWN sequences of the same duration, each time using a controller based on the previously adapted parameters to attenuate the modal response of the beam. Adaptation of the controller parameters continued in this fashion until the sum of the squared errors over each 0.25 sec. excitation interval had decreased to a steady-state level, which was generally between three and six orders of magnitude below the uncontrolled case (i.e., 27 to 60 dB vibration reduction).

As discussed above, *all mode controllers implemented in this study utilized only four parameters; two parameters were used to weight the previous control outputs,* $\hat{c}_m(t-1)$ *and* $\hat{c}_m(t-2)$*, and two to weight previous measurements of the modal displacement of the beam,* $w_m(t-1)$ *and* $w_m(t-2)$. These controllers required approximately 1000 GWN sequences of length 0.25 sec. to achieve the above-stated error reduction, independently of the mode, m, being controlled. This suggests that real-time, off-line training of the network requires approximately four minutes. Note that training is done only once off-line to obtain nominal control parameters for each mode to be controlled; in addition, training of all mode controllers may be performed in parallel. Also, *the coefficients determined in training the controller for each mode were used under all flow conditions. Because the controller is trained on GWN, it is general enough to handle essentially any broadband flow condition.*

Since the plant in the simulation is stationary, no on-line adaptation was required. An adaptive controller may be implemented, however, by continuously observing, on-line, the decrease or increase in the modal response of the beam to parameter changes, as was done during off-line training. In essence, the controller continually searches for new parameters to improve performance. In general, the search space is a nonlinear function of the parameters; thus, search techniques such as GRS may be used. Alternatively, Levenberg-Marquardt (LM) or LMS algorithms may also be used, based on the equations that describe the plant or on-line approximations, respectively. Since the plant equations are well known, or can be learned (e.g., estimated) inductively based on empirical data, an LM algorithm is a practical way to achieve significantly more rapid convergence of the parameters both on- and off-line.

9.2 Beam, Single Mode, Subsonic Flow

9.2.1 Laminar Boundary Layer

For laminar flow, the excitation process $f(t)$ is assumed to be sinusoidal, as discussed in Section 4. Fig. 9.3a illustrates the response of the beam to pure laminar flow when no control is applied, where the sinusoidal excitation frequency was selected to correspond with the resonant frequency of the first mode (*viz.*, 90.86 *Hz*). The amplitude of the excitation was scaled to equal that of the turbulent filter discussed in the next section. From the figure it can be seen that the projection of the beam displacement, w_1, onto the first principal spatial eigenfunction, ψ_1, grows in an oscillatory fashion until a steady state is achieved. Fig. 9.3b illustrates the modal response of the beam when control is applied continuously during beam excitation. Table 9.2 provides the average sum-square modal displacement error of the beam for the first mode, as computed over the last 0.1 sec. of data in the figures. From the table it can be seen that the controller reduces the average sum-squared error of the modal response of the beam by 60.3 dB.

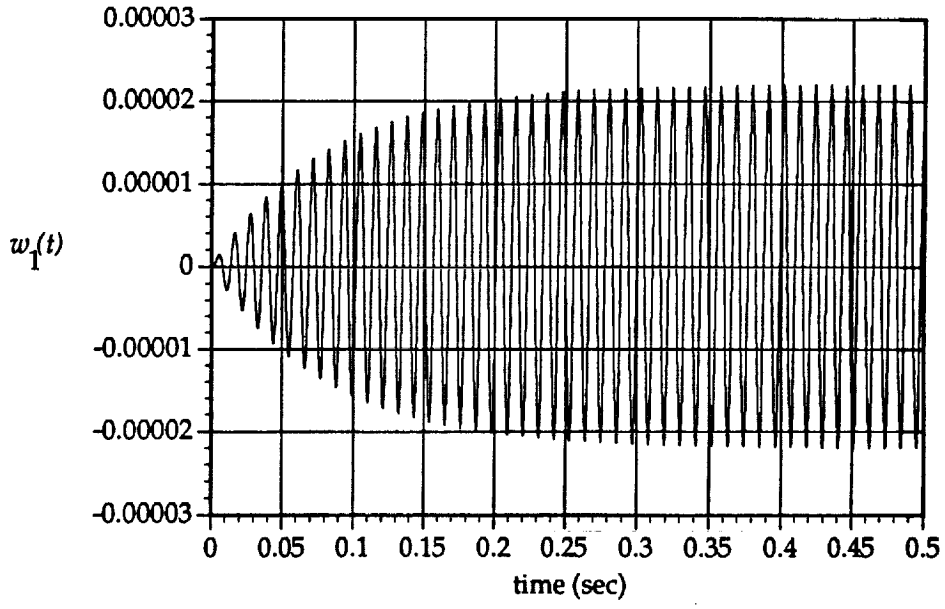

Figure 9.3a: Uncontrolled First Mode Response of Beam to Laminar Excitation

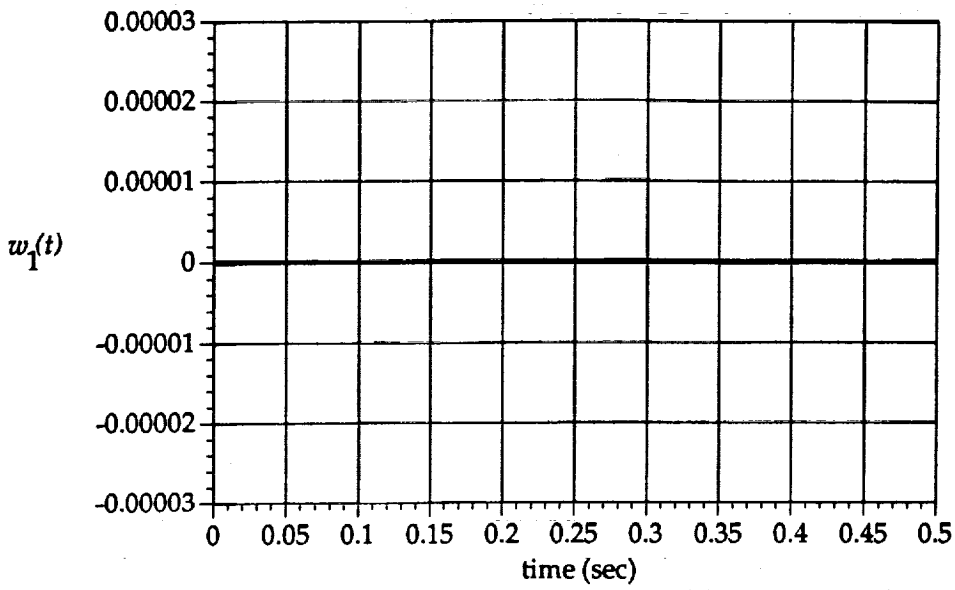

Figure 9.3b: Controlled First Mode Response of Beam to Laminar Excitation; Note that Linewidth has been Increased to Make Response Visible

Table 9.2: Average Sum-Squared Modal Displacement for Mode One with and without Control

Type of Excitation	Average Sum-Squared Error (without Control)	Average Sum-Squared Error (with Control)	Vibration Reduction with Control (dB)
Laminar	2.43134×10^{-10}	2.24831×10^{-16}	60.3
Turbulent	7.25780×10^{-14}	6.70857×10^{-17}	30.3
Transitional	4.87394×10^{-11}	1.64366×10^{-16}	54.7

9.2.2 Turbulent Boundary Layer

In exciting the beam with turbulent flow, a major challenge is to simulate the forcing process. This part of the simulation requires generation of random sequences with the power spectral density of the sampled continuous-time disturbance. For the first mode this spectral density is given by

$$\varphi_d(\omega) = f_S \, \Gamma_{1,1}(f_S \omega), \qquad -\pi < \omega \leq \pi, \tag{9.12}$$

where $\Gamma_{1,1}$ is given in Eq. 7.13. Such a sequence can be generated by filtering a white Gaussian process with a filter whose transfer function is

$$H(\omega) = \sqrt{\varphi_d(\omega)}, \qquad -\pi < \omega \leq \pi. \tag{9.13}$$

This filtering can be performed in the frequency domain, as shown in Fig. 9.4, by first generating a white Gaussian sequence; applying a fast-Fourier transform (FFT); multiplying the transformed sequence by $H(\omega)$; and then retransforming back to the time domain. Implementation of this model directly in the time domain is also straightforward, as will be seen.

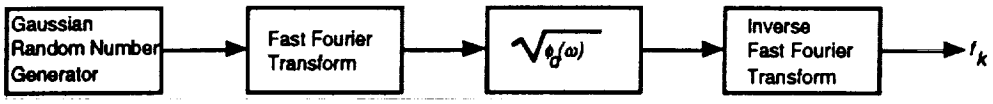

Figure 9.4: Simulation of Turbulent Forcing Function

From Eqs. 7.10 - 7.18, the turbulent forcing function f_1 is seen to be a Gaussian random process with power spectral density:

$$\Gamma_{1,1}(\omega) = 2\,F(\omega)\,[\mathrm{Re}\{\Delta_{1,1}\} + \mathrm{Re}\{\Xi_{1,1}\}], \tag{9.14}$$

where $\Delta_{1,1}$, $\Xi_{1,1}$, and F, are as defined in Eqs. 7.14, 7.15, and 7.17, respectively. The function $F(\omega)$ is plotted versus ω in Fig. 9.5 for the subsonic benchmark parameters. Note that this part of the spectrum is relatively broadband, having a (one-sided) half-power bandwidth of approximately 3000 rad./sec. (500 *Hz*). For reference, the fundamental frequency of the unforced oscillator occurs at 570.9 rad./sec., as shown in Table 9.1.

The remaining term in Eq. 9.14 is a rational function of frequency. Its primary behavior as a function of frequency can be predicted from the function

$$\frac{1}{|A^4 - \lambda_1|} \tag{9.15}$$

as seen in Eqs. 7.14 and 7.15.

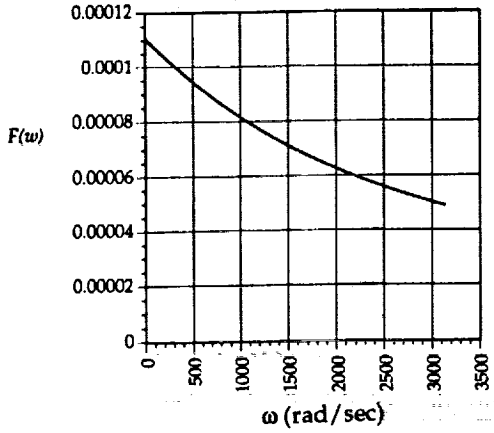

Figure 9.5: F(ω), the "Irrational" Part of the Forcing Spectrum for Subsonic Benchmark Parameters: $\delta^* = 0.0039m$, $v = 110m/s$, $A_1' = 0.24$, $A_2' = 1.08$, $A_3' = 1.80$, $K_1' = 0.47$, $K_2' = 3.0$, and $K_3' = 14.0$

Fig. 9.6 shows the behavior of the real part of the rational term $\Delta_{1,1}$ for the subsonic benchmark parameters. Note that this function has a much narrower bandwidth than that of F; thus, it will determine the overall bandwidth of the forcing function. Fig. 9.7 illustrates the behavior of the real part of the rational term

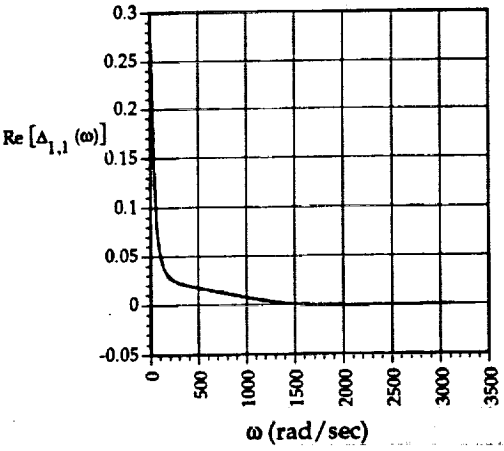

Figure 9.6: Real Part of $\Delta_{1,1}(\omega)$, a Component of the "Rational" Part of Forcing Spectrum for Subsonic Benchmark Parameters: $A = g + iw/U_c$, $g = 1/(U_c\theta)$, $U_c\theta = 17\delta^*$, $U_c = 88m/s$, and $\delta^* = 0.0039m$.

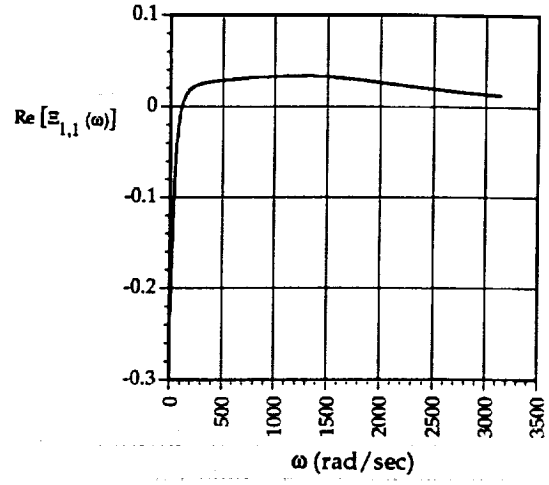

Figure 9.7: Real Part of $\Xi_{1,1}(\omega)$, a Component of the "Rational" Part of Forcing Spectrum for Subsonic Benchmark Parameters: $A = g + iw/U_c, g = 1/(U_c\theta)$, $U_c\theta = 17\delta^*$, $U_c = 88m/s$, and $\delta^* = 0.0039m$.

$\Xi_{1,1}$, again using the subsonic benchmark parameters. The complete turbulent excitation forcing function of Eq. 9.14, which is real everywhere for mode one, is plotted in Fig. 9.8.

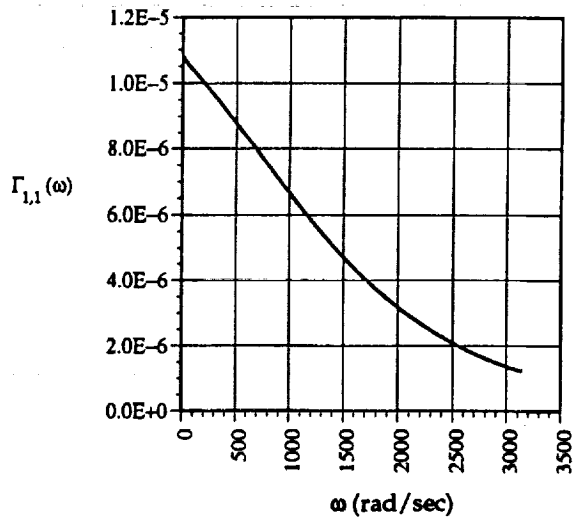

Figure 9.8: Spectral Density of Turbulent Excitation for Mode One Based on Subsonic Benchmark Parameters

It should be noted that, in view of the fact that the function $F(\omega)$ is relatively broadband, a reasonable approximation in computing $\Gamma_{1,1}(\omega)$ would be to assume that $F(\omega)$ is, in fact, constant. This approximation models the forcing process as a rational system driven by white noise. In particular, under this assumption, the spectrum $\Gamma_{1,1}(\omega)$ becomes a ratio of polynomials in ω^2. These polynomials can be factored into causal and anti-causal parts, the causal part of which defines a filter generating the desired forcing process when driven by white Gaussian noise. (see, e.g., Chapter 5 of [16].) This was *not* the approach taken herein, however. As discussed earlier in this section, Eqs. 7.14, 7.15, and 7.17 were solved analytically for the first two modes. These solutions are rather extensive and are therefore not given here; they were generated using *Mathematica*, a software package for performing symbolic (as opposed to numeric) calculations by computer. Instead, their spectra are given graphically: for the first mode, there is a single filter term $\Gamma_{1,1}(\omega)$, which was depicted in Fig. 9.8. This filter was numerically simulated for $-\pi < \omega \leq \pi$, and the inverse Fourier transform computed using an FFT algorithm, to obtain the turbulent excitation impulse response function in the time domain. A white Gaussian sequence was then filtered in the time domain using an FIR filter with this impulse response, to produce the turbulent excitation signal. Fig. 9.9 shows a typical result in exciting the panel with turbulent flow. Note that in the uncontrolled case (Fig. 9.9a), the modal response of the beam achieves a steady state having significantly less modal displacement than was true for the case of laminar flow. When control is continuously applied (Fig. 9.9b), the average sum-squared modal displacement is reduced by 30.3 dB. Fig. 9.10 illustrates the power spectra corresponding to the first mode displacement depicted in Fig. 9.9. Note that the controller attenuates significantly vibration at all frequencies, not only the resonant frequencies, of the beam.

9.2.3 Laminar-to-Turbulent Boundary Layer Transitions

The simulation of the excitation function in transitional flow was performed using a binary gating field that switched intermittently between the two equilibrium boundary layers (i.e., pure laminar flow and pure turbulent flow). The binary gating field was modeled as Markovian in time, with transition statistics depending on the probability of being in either state. For these experiments the probability parameter, p, was set equal to 0.5, indicating equal likelihood of laminar and turbulent flow conditions. Setting p = 0.5 produces the most intermittent flow regime possible with such a simple model.

The result of intermittent flow gating in the uncontrolled case is shown in Fig. 9.11a. When control is applied the response is as given in Fig. 9.11b, where it is seen that the resultant first mode response is reduced by 54.7 dB.

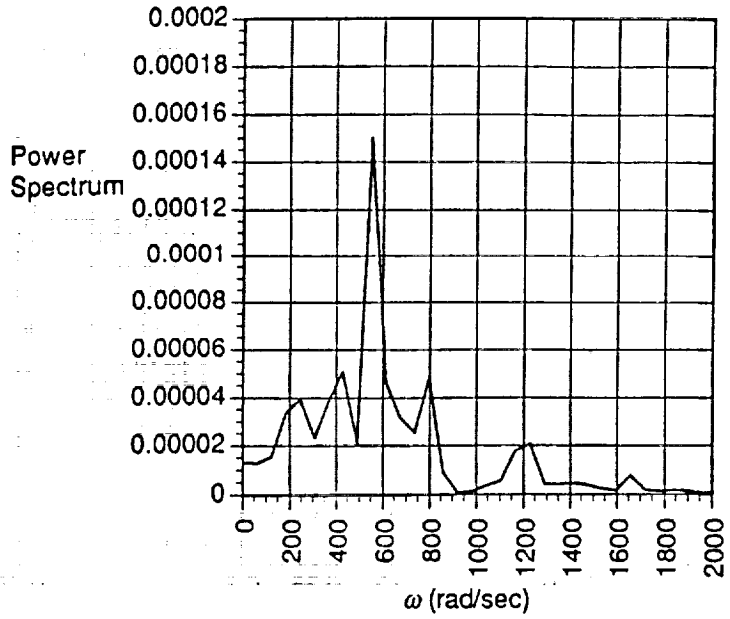

Figure 9.9a: Power Spectrum of Modal Displacement with Turbulent Boundary Layer for Mode One *without* Control

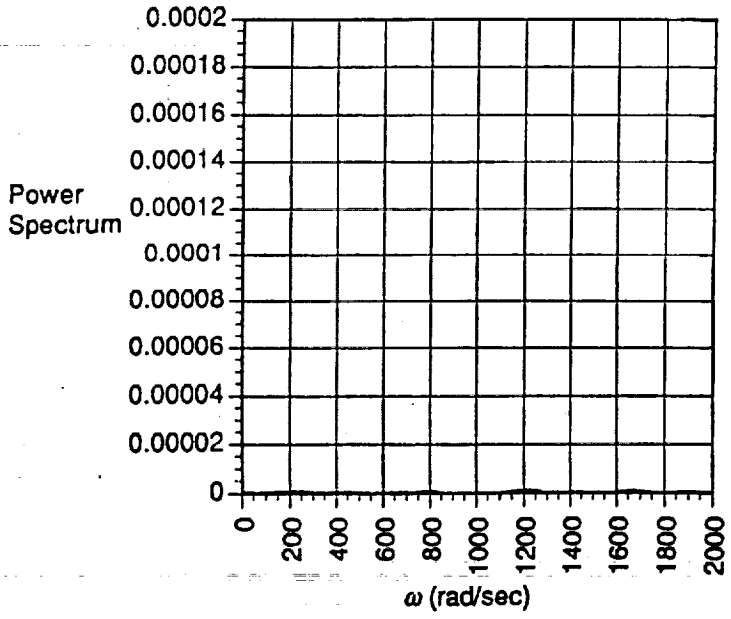

Figure 9.9b: Power Spectrum of Modal Displacement with Turbulent Boundary Layer for Mode One *with* Control

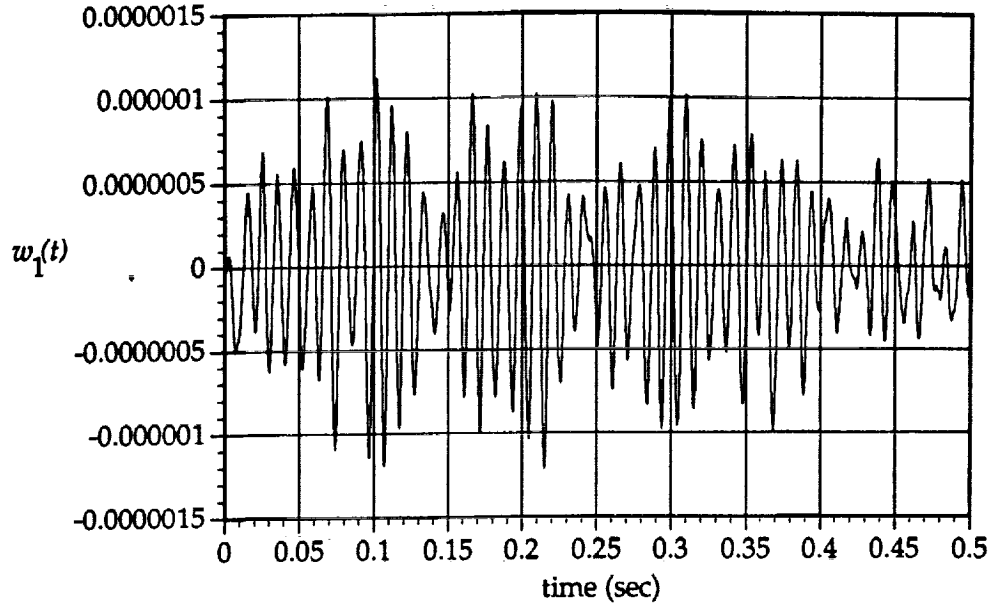

Figure 9.10a: Uncontrolled First Mode Response of Beam to Turbulent Excitation

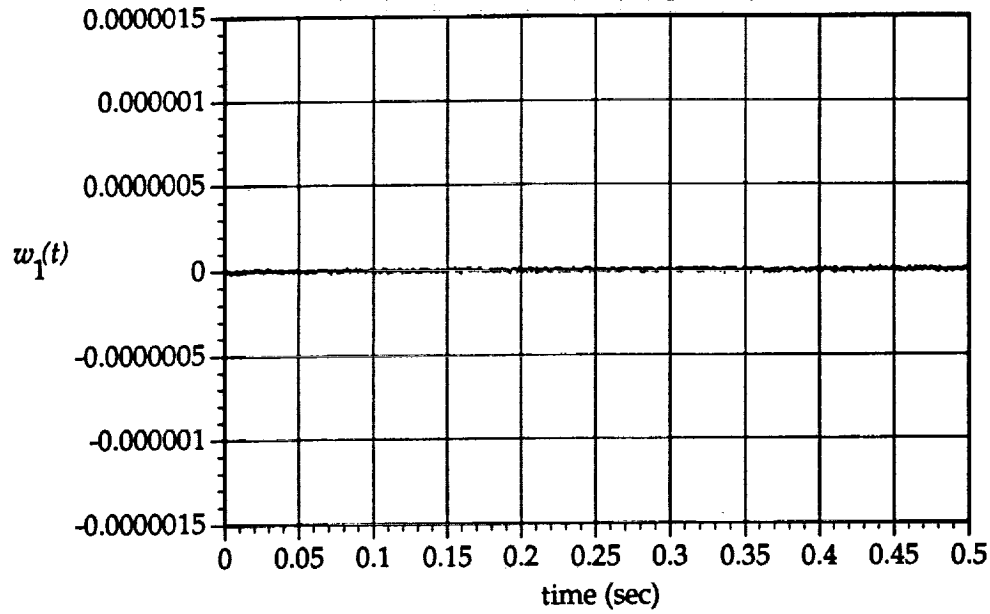

Figure 9.10b: Controlled First Mode Response of Beam to Turbulent Excitation

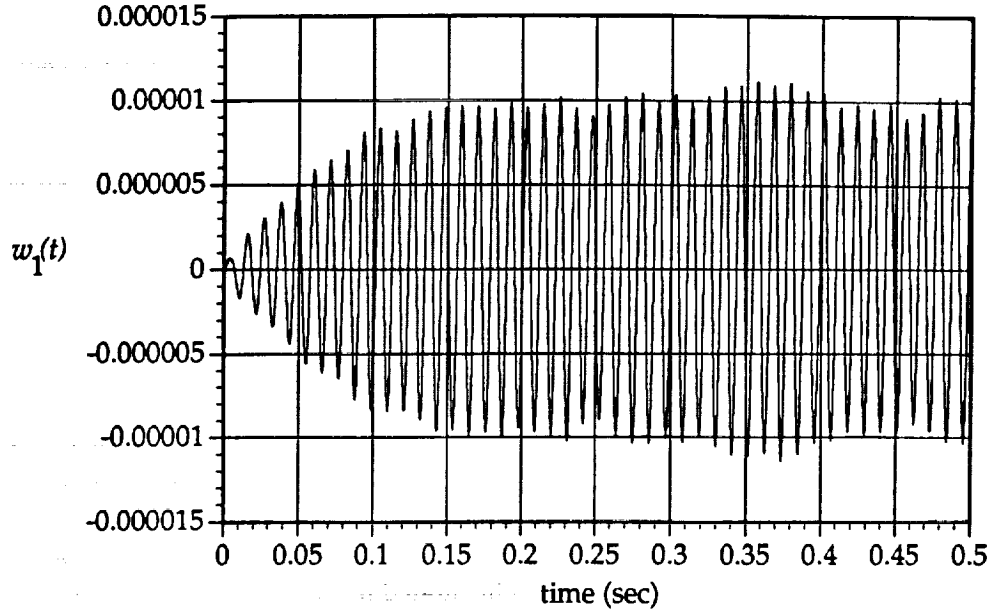

Figure 9.11a: Uncontrolled First Mode Response of Beam to Laminar-to-Turbulent Excitation

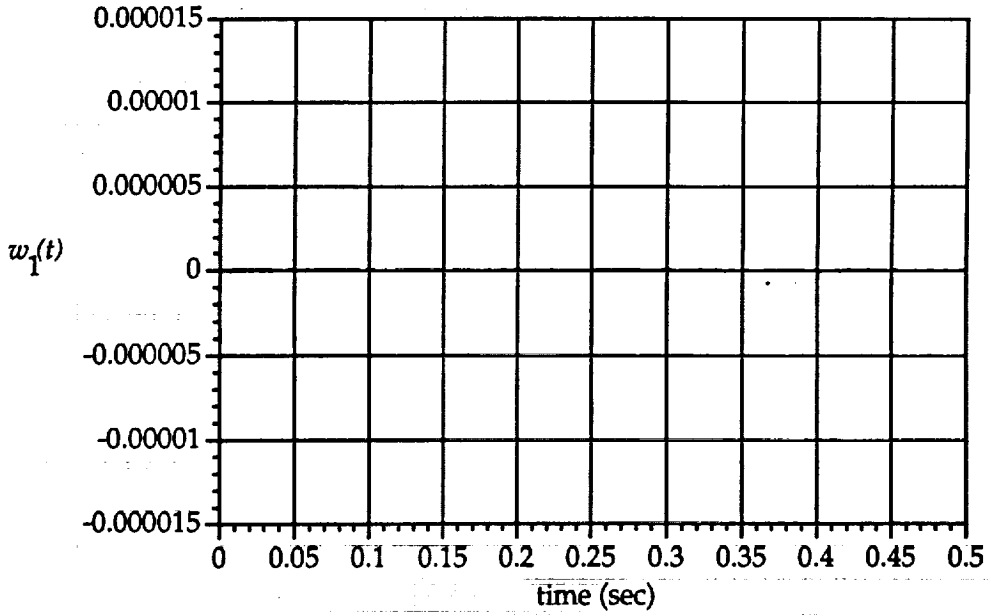

Figure 9.11b: Controlled First Mode Response of Beam to Laminar-to-Turbulent Excitation

As discussed earlier, laminar-to-turbulent boundary-layer transitions represent a non-Gaussian excitation which, in general, will require the use of nonlinear elements in the adaptive PNN controller. In our simulations, however, it was found that linear networks adequately attenuated the modal displacement. We believe that this was the case because each mode of the beam represents a narrowband filter with respect to the broadband turbulent excitation. The bandwidth of a system is inversely proportional to its time constant, and this plant has a relatively large time constant. The consequence is that the effects of the input excitation are averaged in time and therefore tend to a Gaussian distribution, for which case a linear controller is optimal.

9.3 Beam, Multi-Mode, Subsonic Flow

The introduction of multiple modes complicates the above problem in that the scalar Eq. 9.1 is replaced by the vector Eq. 5.1. The turbulent forcing field then is a vector Gaussian process with a spectral density matrix described as in Eqs. 7.14, 7.15, and 7.17. The control is now a vector process and the adaptation becomes a vector adaptation. For the various flow conditions illustrated below, results are provided for the second mode only since the vibration attenuation in each mode is essentially independent of the other modes; therefore, results obtained for the second mode were similar to those demonstrated above for the case of single-mode control.

9.3.1 Laminar Boundary Layer

Laminar flow was again simulated as a sinusoidal process, this time with a frequency equal to that of the resonant frequency of the second mode of the beam (*viz.*, 250.46 *Hz*). Fig. 9.12a illustrates the response of the second mode of the beam to laminar flow when no control is applied. The projection of the beam displacement, w_2, onto the second principal spatial eigenfunction, ψ_2, of the beam grows until it achieves a steady state. The response of the beam when control is applied is shown in Fig. 9.12b. From Table 9.3 it can be seen that the average vibration reduction as computed over the last 0.1 sec. of the data was reduced by 51.0 dB.

9.3.2 Turbulent Boundary Layer

To simulate turbulent flow, Eqs. 7.14, 7.15, and 7.17 were solved analytically for Γ. For the second mode, Γ is a matrix of dimension 2×2 that cross-couples the random processes exciting each mode independently; specifically, the boundary-layer forces are generated using the following equation:

$$\begin{bmatrix} f_1 \\ f_2 \end{bmatrix} = \begin{bmatrix} \Gamma_{1,1} & \Gamma_{1,2} \\ \Gamma_{2,1} & \Gamma_{2,2} \end{bmatrix} \begin{bmatrix} GWN_1 \\ GWN_2 \end{bmatrix} \tag{9.16}$$

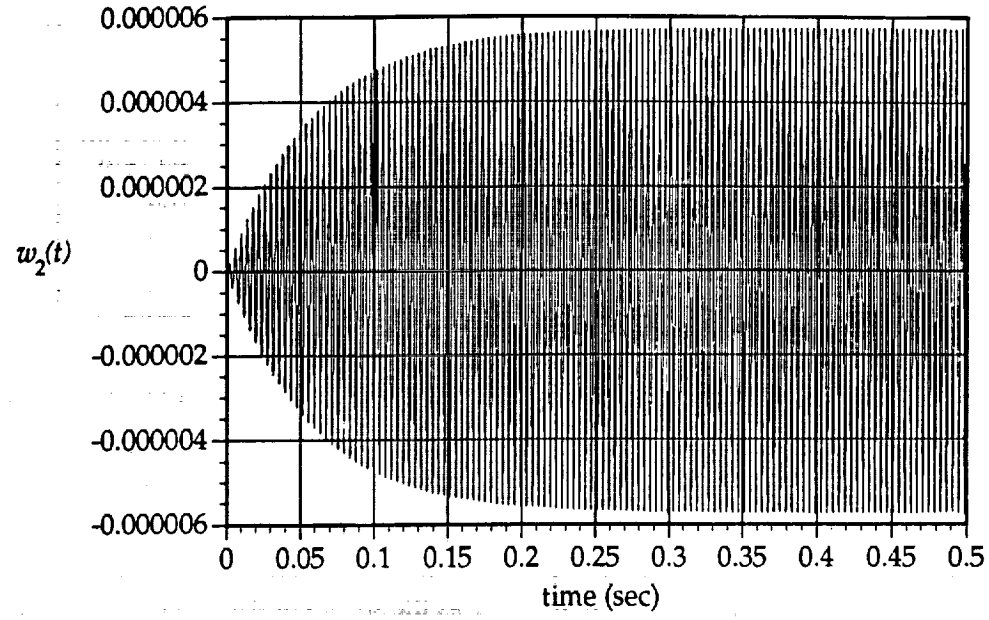

Figure 9.12a: Uncontrolled Second Mode Response of Beam to Laminar Excitation

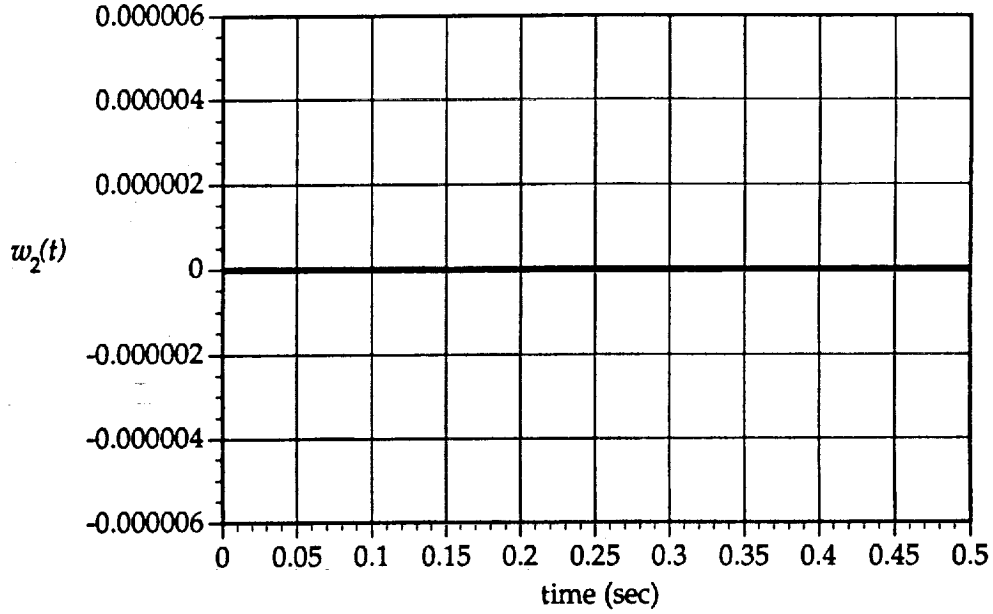

Figure 9.12b: Controlled Second Mode Response of Beam to Laminar Excitation; Note that Linewidth has been Increased to Make Response Visible

Table 9.3: Average Sum-Squared Modal Displacement for Mode Two with and without Control

Type of Excitation	Average Sum-Squared Error (without Control)	Average Sum-Squared Error (with Control)	Vibration Reduction with Control (dB)
Laminar	1.64807×10^{-11}	1.29531×10^{-16}	51.0
Turbulent	8.25576×10^{-14}	6.62533×10^{-17}	31.0
Transitional	4.68968×10^{-12}	1.34811×10^{-16}	45.4

where GWN_1 and GWN_2 are independent Gaussian white noise processes. Note that in the unimodal case, $GWN_2 = 0$, so that only the $\Gamma_{1,1}$ term was needed. In the multimodal case, creating the turbulent excitation amounts to filtering independent GWN sequences using the multi-dimensional filter Γ.

For the second mode there are four terms in the spectral density matrix; in general, for m modes, the matrix has m^2 terms, growing as the square of the number of modes. As m increases, the analysis and computational effort to generate the turbulent forcing functions having the appropriate spectral characteristics grows dramatically. For this reason, the number of modes studied in this Phase I report was limited to the first two.

As mentioned earlier, the individual terms of Γ, namely $\Gamma_{1,1}$, $\Gamma_{1,2}$, $\Gamma_{2,1}$, and $\Gamma_{2,1}$, were generated based on Eqs. 7.14, 7.15, and 7.17. The spectral density $\Gamma_{1,1}$ was discussed earlier in Section 9.2.2 in describing the turbulent excitation for mode one; recall that $\Gamma_{1,1}$ in Eq. 9.14 is real because the imaginary terms cancel in Eq. 7.13; this is guaranteed in this case because $\Delta_{i,j} = \Delta_{j,i}$ and $\Xi_{i,j} = \Xi_{j,i}$. For the same reason, $\Gamma_{2,2}$ will also be real; Fig. 9.13 shows a graph of $\Gamma_{2,2}(\omega)$ vs. ω. The remaining terms in the turbulent filter matrix Γ are $\Gamma_{1,2}$ and $\Gamma_{2,1}$, which are complex since the imaginary terms do not cancel, because in general $\Delta_{i,j} \neq \Delta_{j,i}$ and $\Xi_{i,j} \neq \Xi_{j,i}$; indeed, $\Gamma_{1,2}$ and $\Gamma_{2,1}$ are complex conjugates of one another, so that their imaginary parts add rather than cancel. Graphs of the real and imaginary parts of $\Gamma_{1,2}$ and $\Gamma_{2,1}$ are given in Figs. 9.14 and 9.15 respectively. Note from Eq. 9.16 that the forcing vector f is complex. Because we require a real excitation sequence, only the real parts of $\Gamma_{1,2}$ and $\Gamma_{2,1}$ were used to generate the off-diagonal elements in the turbulent excitation matrix. The Γ matrix was simulated as described earlier to create time-domain filters that were applied to the Gaussian white noise sequences.

Fig. 9.16a illustrates the case of no control for the second mode where the beam was excited using the simulated turbulent flow process defined by Γ. The corresponding controlled case is shown in Fig. 9.16b, where the vibration is seen to have been attenuated by 31.0 dB. The corresponding natural and controlled vibration spectra for this mode are shown in Fig. 9.17.

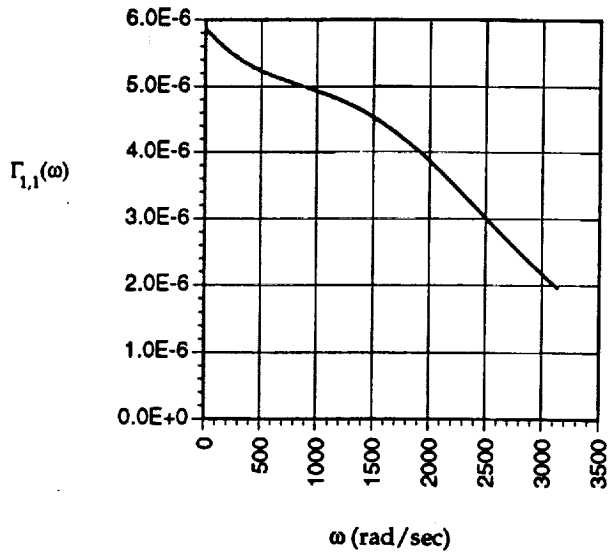

Figure 9.13: Spectral Density Matrix Term $\Gamma_{2,2}$

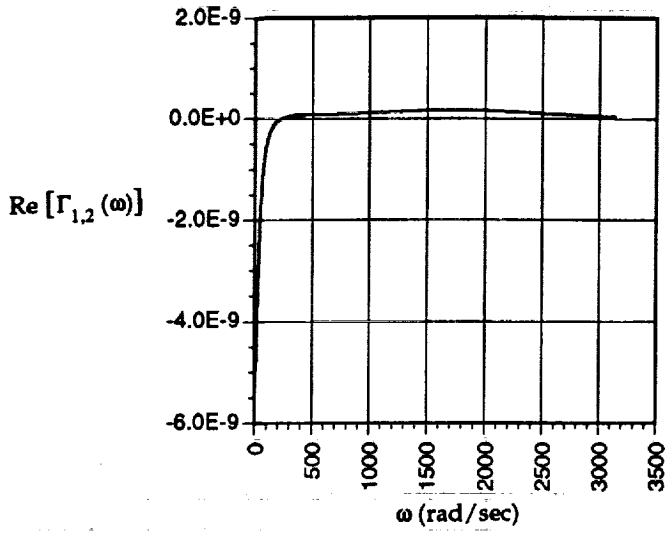

Figure 9.14a: Real Part of Spectral Density Matrix Term $\Gamma_{1,2}$

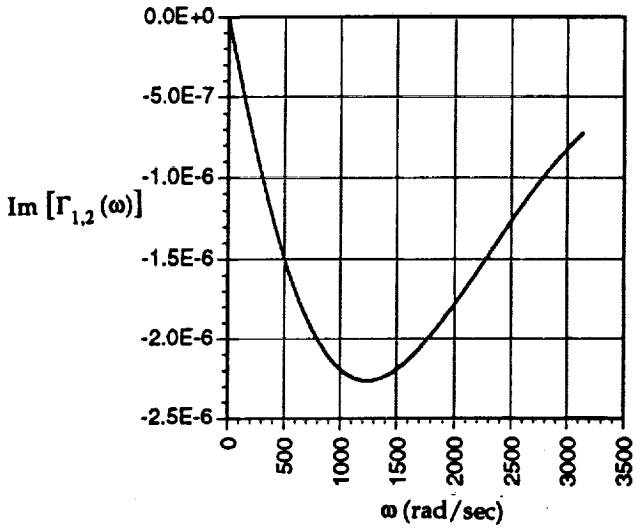

Figure 9.14b: Imaginary Part of Spectral Density Matrix Term $\Gamma_{1,2}$

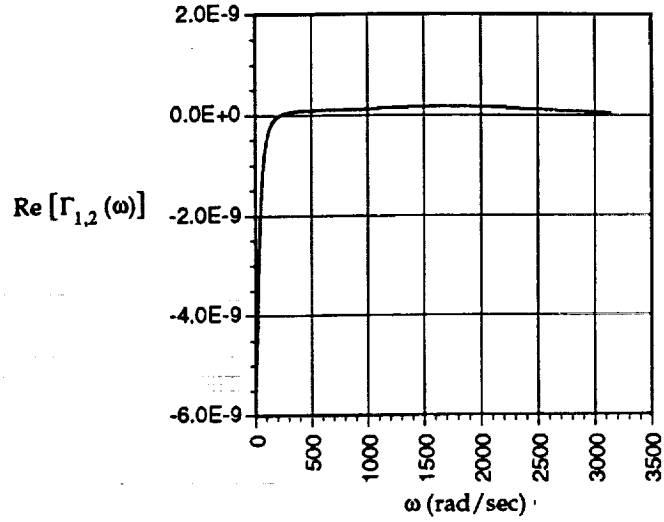

Figure 9.15a: Real Part of Spectral Density Matrix Term $\Gamma_{2,1}$

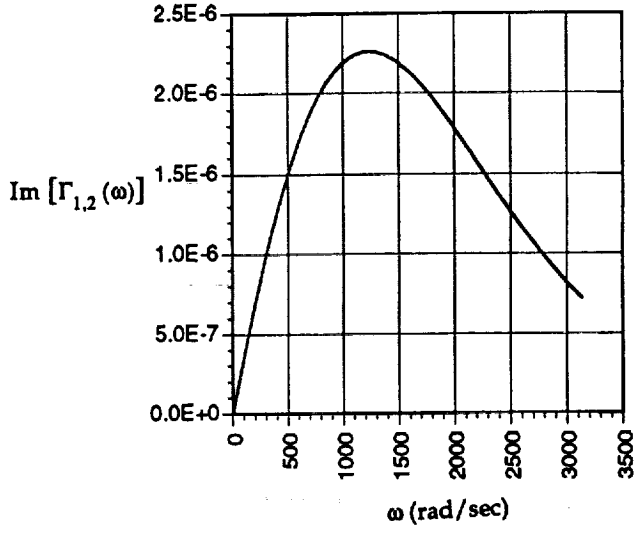

Figure 9.15b: Imaginary Part of Spectral Density Matrix Term $\Gamma_{2,1}$

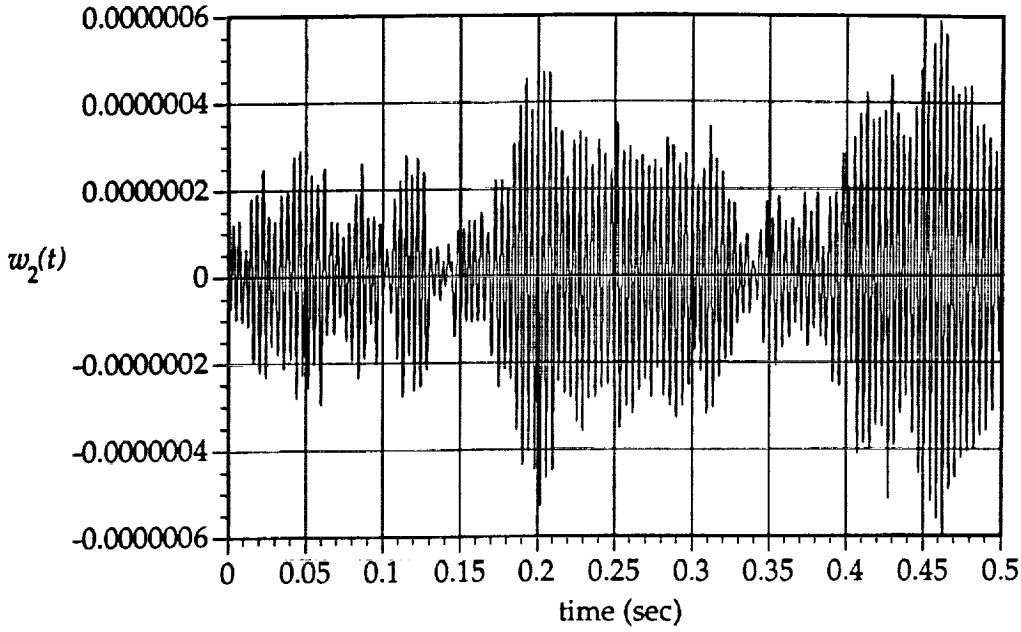

Figure 9.16a: Uncontrolled Second Mode Response of Beam to Turbulent Excitation

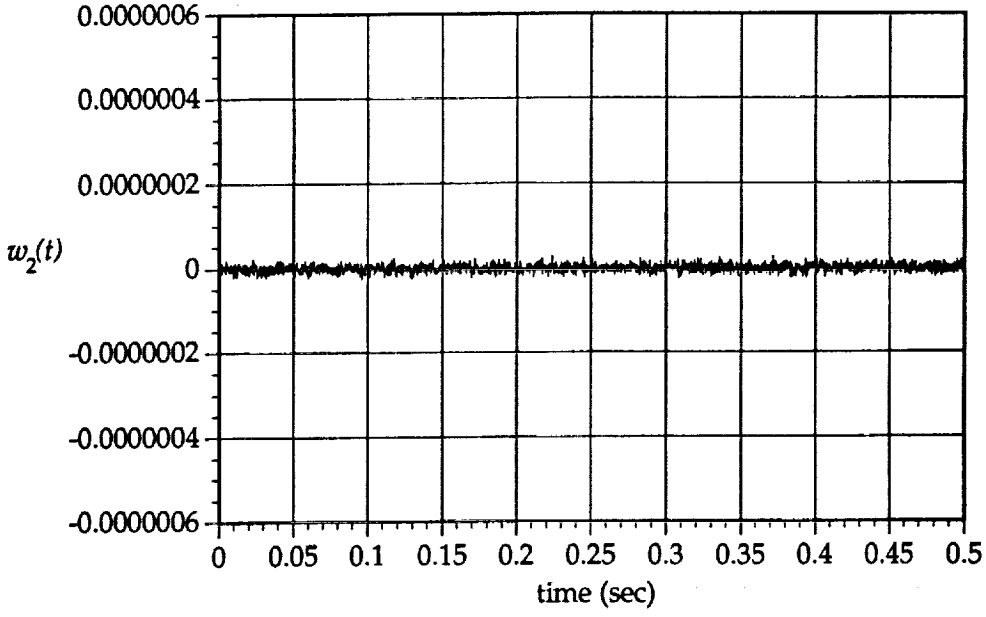

Figure 9.16b: Controlled Second Mode Response of Beam to Turbulent Excitation

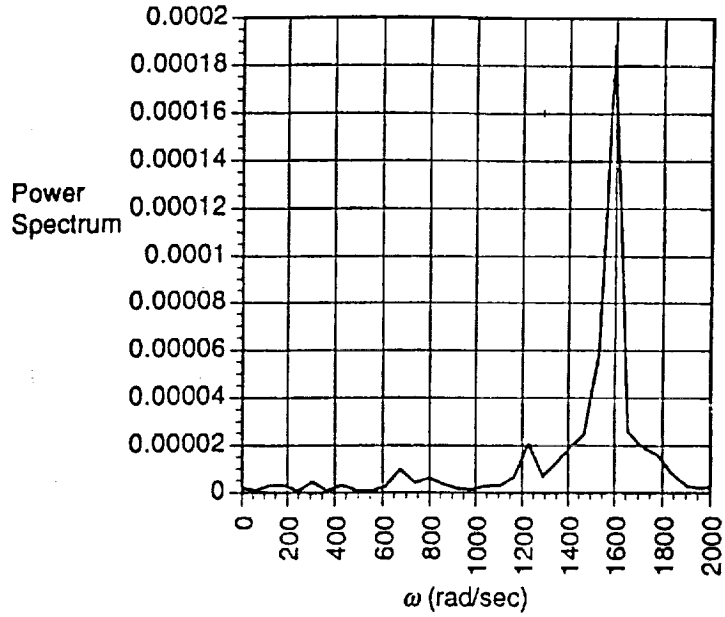

Figure 9.17a: Power Spectrum of Modal Displacement with Turbulent Boundary Layer for Mode Two *without* Control

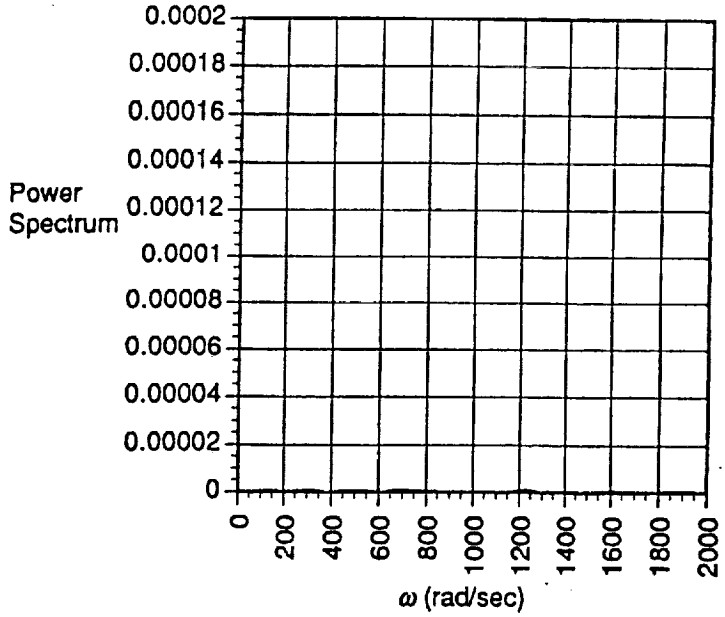

Figure 9.17b: Power Spectrum of Modal Displacement with Turbulent Boundary Layer for Mode Two *with* Control

9.3.3 Laminar-to-Turbulent Boundary Layer Transitions

To simulate laminar-to-turbulent boundary layer transitions, the same binary gating field discussed in Section 9.2.3 was used. The response of the second mode of the beam with no control is illustrated in Fig. 9.18a. The controlled case is shown in Fig. 9.18b, where it can be seen that the vibration response has been reduced by 45.4 dB.

9.4 Vibration Suppression as a Function of Damping

To study the reduction in modal displacement in turbulent flow as a function of damping, the damping ratio, ζ, used in the plant model was varied from 0.001 to 0.1. Typically, the range of damping ratios that one would expect to see in panels is on the order of 0.001 to 0.01. The controller polynomial neural network was trained using the power-law proportional damping relationship that is discussed in Section 3 and in Appendices A and B; the trained controller was then tested on plants having different levels of damping. As demonstrated in Appendix B, power-law proportionate damping provides an effective damping ratio of $\zeta_1 = 0.007265$ at the first-mode resonant frequency, and $\zeta_2 = 0.003696$ at the second-mode resonant frequency. Figs. 9.19a and 9.19b illustrate, for the first two modes respectively, that the reduction in vibrational energy due to active control decreases with increasing damping ratio, as passive damping alone reduces the amplitude of vibration to be controlled.

It is interesting to note that even in the case of no damping, the controller is still able to keep vibration to a negligible level, similar to that demonstrated in Sections 9.2 and 9.3. In the undamped case without control, the modal displacement continues to grow without bound for the case of intermittent flow with $p = 0.5$, as shown in Figs. 20a and 21a for the first and second modes respectively; with control, the modal displacement remains negligible, as illustrated in Figs. 20b and 21b. As a result, the relative reduction in vibration level increases without bound as damping goes to zero. Note that the controller in the above undamped case was trained using power-law proportionate damping; it was *not* retrained for the undamped plant. Similar results were obtained for the cases of pure laminar and pure turbulent flow.

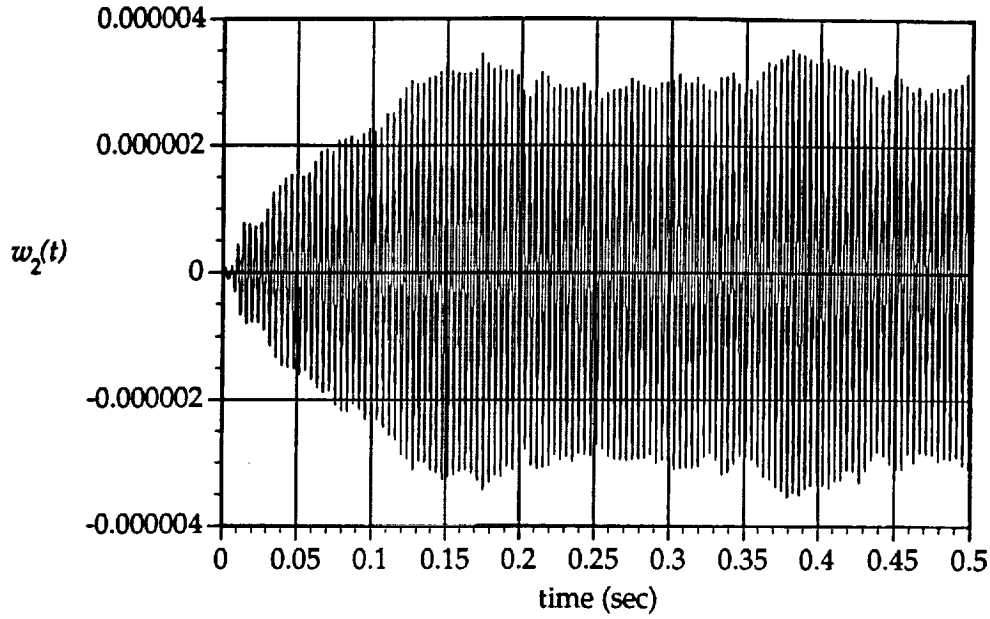

Figure 9.18a: Uncontrolled Second Mode Response of Beam to Laminar-to-Turbulent Transitional Flow

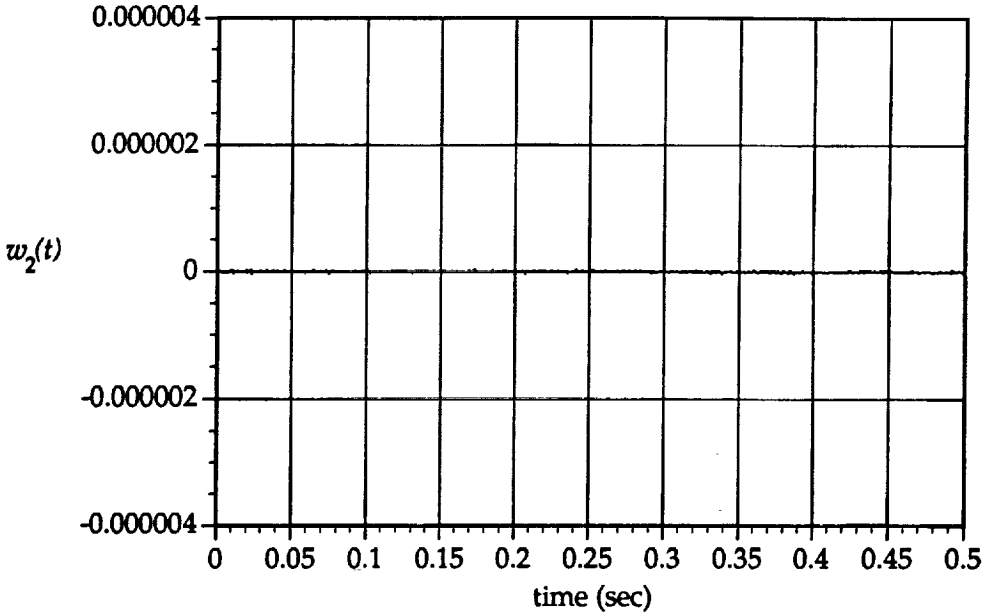

Figure 9.18b: Controlled Second Mode Response of Beam to Laminar-to-Turbulent Transitional Flow

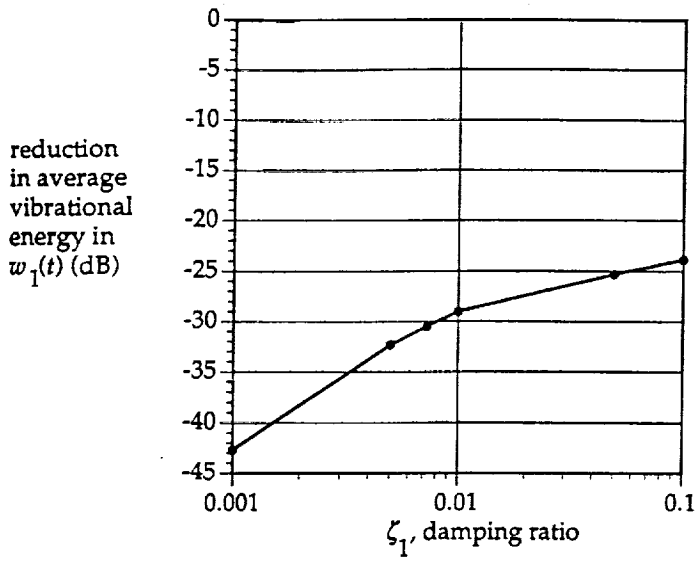

Figure 9.19a: Reduction in Average Vibrational Energy in First Mode with Turbulent Flow

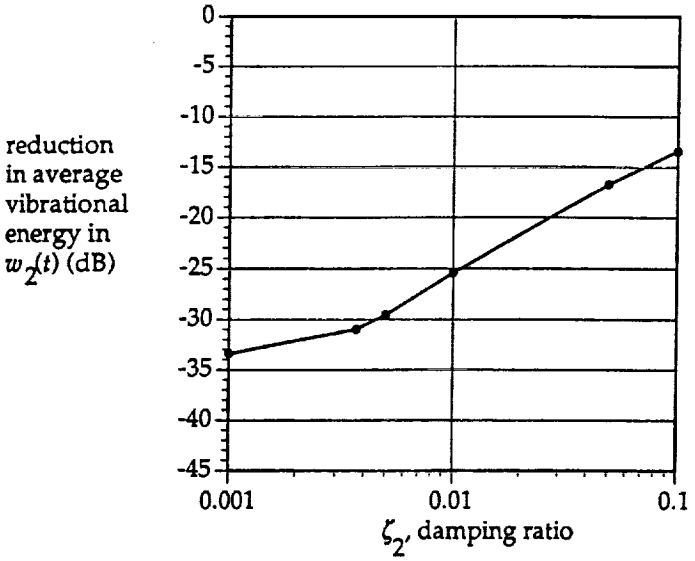

Figure 9.19b: Reduction in Average Vibrational Energy in Second Mode with Turbulent Flow

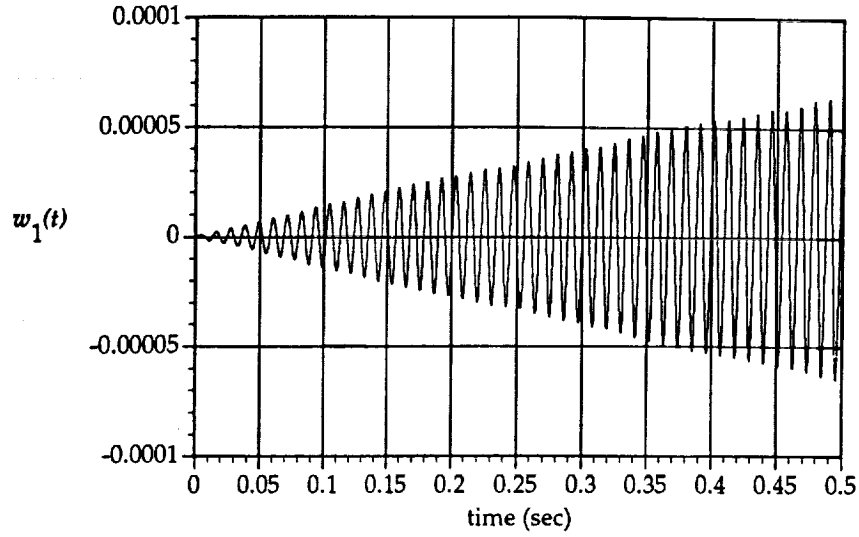

Figure 9.20a. Uncontrolled First Mode Response of Beam to Laminar-to-Turbulent Transitional Excitation with Zero Damping

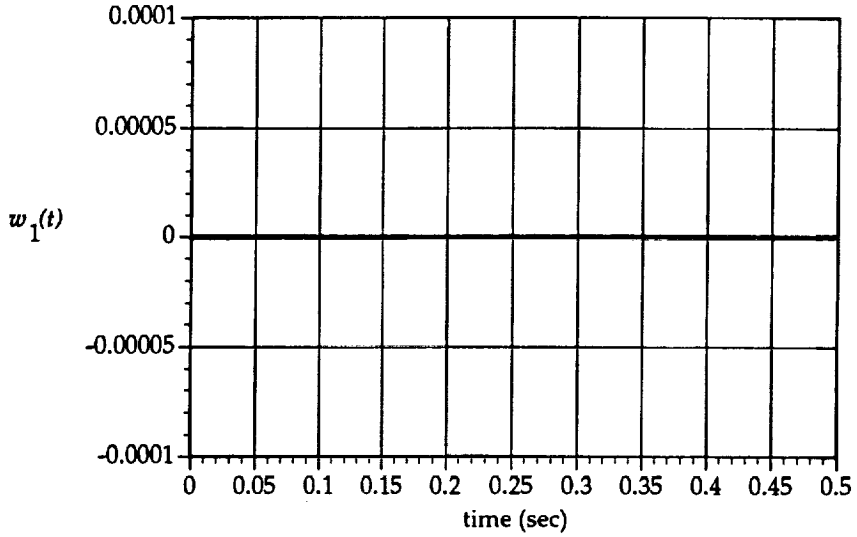

Figure 9.20b. Controlled First Mode Response of Beam to Laminar-to-Turbulent Transitional Excitation with Zero Damping; Note that Linewidth has been Increased to Make Response Visible

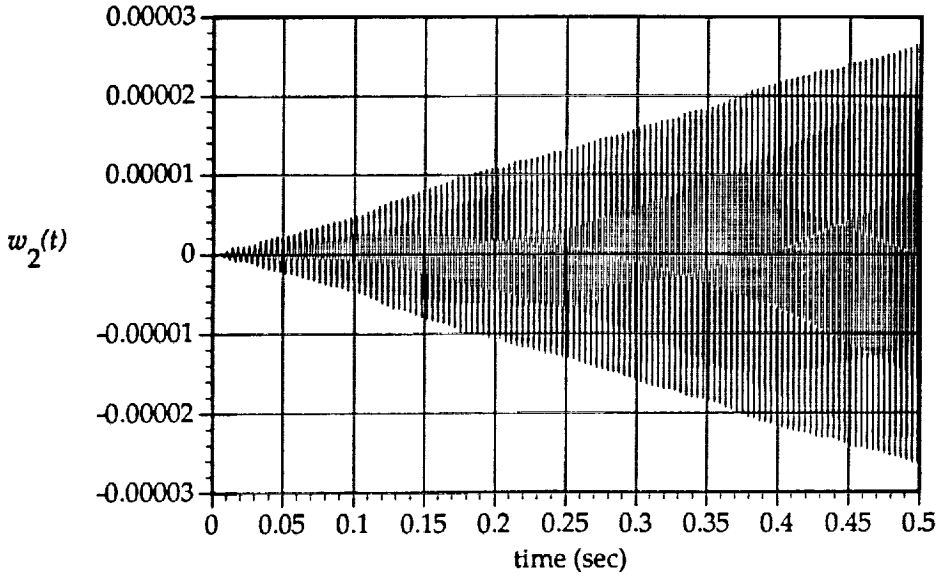

Figure 9.21a: Uncontrolled Second Mode Response of Beam to Laminar-to-Turbulent Transitional Excitation with Zero Damping

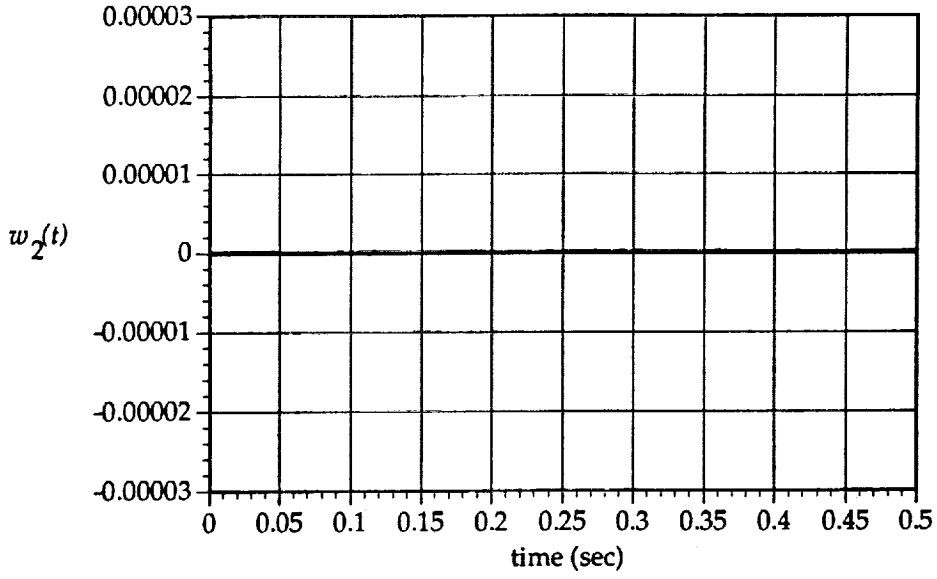

Figure 9.21b: Controlled Second Mode Response of Beam to Laminar-to-Turbulent Transitional Excitation with Zero Damping; Note that Linewidth has been Increased to Make Response Visible

10 Conclusions

Adaptive nonlinear polynomial neural networks were used to control vibration of a simulated aircraft structure (*viz.*, beam) resulting from acoustic excitation by the fluid boundary layer. The objective was to control actively the coupling of sound from the fluid to the structure. The acoustic excitation in this project included laminar, turbulent, and laminar-to-turbulent transitional flows, representing respectively, narrowband-Gaussian, broadband-Gaussian, and broadband-non-Gaussian excitation. Excellent attenuation of 30 to 60 dB was achieved, even under conditions of no natural damping.

11 Future Extensions

11.1 Theoretical Analysis

Due to the necessarily limited scope of the Phase I study, the concept demonstration was restricted to a simpler, lower-dimensional framework than can be reliably used to model actual aircraft panels. To bring the promise of active vibration control into practice, it is necessary to continue this study using more realistic panel models, and to verify the predicted control capabilities through experiment. The following are among the topics to be investigated further:

11.1.1 Plate (versus Beam) Models

The Phase I effort focused on the problem of a vibrating beam rather than a vibrating plate, the latter of which more accurately models aircraft panels. Thus, to bring these techniques to the point of applicability, it is necessary to add an additional (transverse) dimension to the structure being controlled. There are three primary issues that will arise because of this increase in dimensionality. One issue is that, unlike the case of a clamped beam, the eigenstructure of a clamped plate is not known in terms of readily calculated functions. This is primarily an analytical problem that can be overcome using approximation techniques. Another, more substantive, issue is that there may be effects in the control of a vibrating plate that do not appear in a vibrating beam. A further issue is that the possible configurations of discrete actuators and sensors (discussed below) will be quite large; thus, considerable investigation will be necessary to select optimal geometries.

11.1.2 Panel Nonlinearity

The linear plate equation only approximates the true dynamics of a vibrating plate. This approximation is accurate for small deflections and linear-elastic materials where shear distortions and rotary inertia are negligibly small. Thus, in the problem of interest here, this approximation should be accurate for vibrations that cause small panel displacements. If the plate vibration is regulated effectively, a linear model will provide an accurate description of nominal plate behavior. On the other hand, even in a regulated plate, there is the potential for larger plate excursions if the excitation field is sufficiently intense. Such excursions will drive the plate into nonlinear behavior, and thus it is of interest to model this nonlinearity and to consider its effects on controller design and performance. The mathematical modeling of nonlinear plate behavior has been described in several works, including [3, 7]. There are several potential sources of nonlinearity in the plate behavior. Perhaps the most important of these phenomena for the thin, clamped panels often used in aircraft is *in-plane stretching*, which causes additional stiffness when the panel deflection is significant relative to the plate thickness. This stiffness increases with displacement, thereby introducing nonlinearity. For sufficiently large displacements (relative to plate thickness), this membrane action can actually dominate the bending action described by the linear plate equation. This phenomenon can be modeled mathematically using classical equations developed by von Karman [3]. In particular, the plate equation for larger deflections is obtained by adding a bilinear term to the right-hand-side of the linear plate Eq. 2.1. This term is given by:

$$\delta_p \left[\frac{\partial^2 F}{\partial y^2} \frac{\partial^2 w}{\partial x^2} + \frac{\partial^2 F}{\partial x^2} \frac{\partial^2 w}{\partial y^2} - 2 \frac{\partial^2 F}{\partial x \partial y} \frac{\partial^2 w}{\partial x \partial y} \right], \tag{11.1}$$

where δ_p is the thickness of the plate, and F is *Airy's stress function*, which is quadratically related to the deflection w through the PDE:

$$\nabla^4 F = E \left[\left(\frac{\partial^2 w}{\partial x \partial y} \right)^2 - \frac{\partial^2 w}{\partial x^2} \frac{\partial^2 w}{\partial y^2} \right], \tag{11.2}$$

with E denoting Young's modulus.

Subsequent efforts should consider these and related nonlinear phenomena both in terms of their effects on the linear control of vibrating panels, and in terms of their use in the design of appropriate nonlinear active vibration control laws for situations in

which the linear designs fail to exhibit robustness with respect to this nonlinear behavior. For weak nonlinearity, perturbations on the modal approach are suitable for analysis of these problems. However, to simulate accurately the behavior of a strongly nonlinear plate, it may be necessary to abandon the eigenfunction methods that are useful in the linear model and go instead to finite-difference methods of propagating the corresponding nonlinear PDEs. Such simulation methods will also be useful in other aspects of the follow-on studies.

11.1.3 Accurate Sensor/Actuator Models

Practical sensors (e.g., polyvinylidene fluoride (PVDF) films) measure strain rather than displacement, and the control effects produced by practical actuators (e.g., lead-zirconate-titanate (PZT) ceramics) are bending moments rather than direct counterforces to the boundary layer. Although it is possible to produce sensors and actuators that couple into the fixed spatial modes of a plate (see, for example, [2, 6, 10, 14, 23]), a more likely situation is that discrete sensors and actuators will be used. To increase the realism of analytical phases of control design and performance prediction, it is necessary to consider the constraints imposed by such physical sensors and actuators. Use of multiple sensors and actuators represents a first step toward systems that can be practically implemented.

As a more realistic measurement model, we consider here the sensing/actuation of the field by discrete sensors/actuators having non-negligible dimensions, placed on the surface of the beam. (For the purposes of discussion, we consider a beam model.) One immediate effect of such a model is that, unlike the distributed case, it will not be possible to isolate modes in this context, and thus modal coupling through the controller must be considered. To model this situation, it is convenient to represent the dynamics of the beam in terms of an infinite-dimensional state-space model:

$$\dot{\underline{X}}_t = \mathbf{A}\,\underline{X}_t + \mathbf{B}\,\underline{f}_t \tag{11.3}$$

where the state vector $\underline{X}_t$ is given by

$$\underline{X}_t = \begin{bmatrix} w_1(t) \\ \dot{w}_1(t) \\ w_2(t) \\ \dot{w}_2(t) \\ \vdots \\ \vdots \end{bmatrix}$$

with $w_k(t)$ and $\dot{w}_k(t)$ denoting the k^{th} mode of the displacement field and its time derivative, respectively, i.e., $w_k(t) = \int_0^a w(x,t)\ \psi_k(x)\ dx$. **A** denotes the block-diagonal matrix with 2×2 diagonal block

$$\mathbf{A} = \begin{bmatrix} 0 & 1 \\ -\omega_k^2 & -2\zeta_k\omega_k \end{bmatrix}$$

with $\omega_k = \sqrt{D\ \lambda_k/\rho_1}$. As before, D denotes the beam stiffness, ρ_1 its mass density per unit length, λ_k is the k^{th} eigenvalue of the operator $\frac{\partial^4}{\partial x^4}$, ζ_k the damping ratio for the k^{th} mode, and f_t denotes the vector whose k^{th} component is the projection of the boundary layer pressure field onto the k^{th} mode of the beam (i.e., $f_k(t) = \int_0^a f(x,t)\ \psi_k(x)\ dx$); **B** is the matrix

$$\mathbf{B} = \begin{pmatrix} 0 & 0 & 0 & 0 & \dots \\ 1 & 0 & 0 & 0 & \dots \\ 0 & 0 & 0 & 0 & \dots \\ 1 & 0 & 0 & 0 & \dots \\ 0 & 0 & 0 & 0 & \dots \\ 1 & 0 & 0 & 0 & \dots \\ . & . & . & . & \dots \end{pmatrix}.$$

Note that the modes are *a fortiori* uncoupled in this model; and, with the above model based on perfect sensing and actuation, the modes remain uncoupled. On the other hand, if the beam motion is observed and actuated through practical sensors and actuators, mode-coupling will result.

Suppose the beam motion is observed through a sensor occupying the region $\{x_0 \le x \le x_1\}$ with $0 \le x_0 < x_1 \le a$. The resulting sensor electrical signal $r(t)$ equals $K \int_{x_0}^{x_1} s(x,t)dx$, where $s(x,t)$ is the strain in the beam and K is a constant incorporating the efficiency of the sensor in converting strain into electrical energy. The strain is related through the displacement by

$$s(x,t) = K' \frac{\partial^2 w(x,t)}{\partial x^2}, \qquad (11.4)$$

where K' is a constant determined by the properties of the panel material. Thus, the sensor signal is given by

$$r(t) = K_s[w_x(x_1,t) - w_x(x_0,t)], \tag{11.5}$$

where $w_x = \dfrac{\partial w(x,t)}{\partial x}$ and $K_s = K\,K'$.

Since $w(x,t) = \sum_{k=1}^{\infty} w_k(t)\psi_k(x)$, the sensor signal can be written in terms of the state $\underline{X}_t$ as

$$r(t) = \underline{h}\ \underline{X}_t \tag{11.6}$$

where $\underline{h} = K_s\,[(\psi_{1,x}(x_1) - \psi_{1,x}(x_0)),\ \ 0,\ \ (\psi_{2,x}(x_1) - \psi_{2,x}(x_0)),\ \ 0,\ \ \ldots]$ with $\psi_{k,x} = \dfrac{\partial}{\partial x}\psi_k$. Obviously, if we have multiple sensors, each one will satisfy such an equation. Thus, with L sensors we have a measurement equation:

$$\begin{pmatrix} r_1(t) \\ r_2(t) \\ \vdots \\ r_L(t) \end{pmatrix} = \mathbf{H}\underline{X}_t \tag{11.7}$$

with

$$\mathbf{H} = \begin{pmatrix} \underline{h}_1 \\ \underline{h}_2 \\ \vdots \\ \underline{h}_L \end{pmatrix}, \tag{11.8}$$

and $\underline{h}_l$ denoting the l^{th} version of $\underline{h}$ above.

Similarly, practical actuation can be modeled as follows. An electrical signal into an actuator occupying the region $y_0 \le x \le y_1$ will produce a bending moment whose

magnitude is directly proportional to the voltage applied to the actuator; i.e., $M(t) = K_a c(t)$, where $c(t)$ is the control voltage across the actuator leads. (Formulas relating the constant K_a to the material properties and geometry of the actuator are available.) This moment can be modeled as consisting of two equal-magnitude bending moments around the endpoints, y_0 and y_1, of the actuator. These bending moments can be taken to act in opposite directions so as to bend the center of the actuator down. In terms of forces driving the beam equation, these moments can be represented as four point forces, each having magnitude $\frac{M(t)}{2\Delta x}$, located at the points $x = y_0 - \Delta x$, $x = y_0 + \Delta x$, $x = y_1 - \Delta x$, and $x = y_1 + \Delta x$, where $\Delta x > 0$ is small relative to the sensor dimension. The forces at $x = y_0 - \Delta x$ and $x = y_1 + \Delta x$ are upward, and the forces at $x = y_0 + \Delta x$ and $x = y_1 - \Delta x$ are downward. Thus, the force created by the control signal $c(t)$ applied to the actuator becomes

$$f_a(x,t) = \frac{K_a c(t)}{2\Delta x}[\delta(x - y_0 - \Delta x) - \delta(x - y_0 + \Delta x) + \delta(x - y_1 + \Delta x) - \delta(x - y_1 - \Delta x)], \qquad (11.9)$$

where $\delta(\cdot)$ denotes the Dirac delta function.

As an input to the beam state equation, this force translates into a vector $f_a(t)$ with k^{th} component (i.e., input to the k^{th} mode)

$$f_{a,k}(t) = \int_0^a f_a(x,t)\psi_k(x)dx = \frac{K_a c(t)}{2\Delta x}[\psi_k(y_0 + \Delta x) - \psi_k(y_0 - \Delta x) + \psi_k(y_1 - \Delta x) - \psi_k(y_1 + \Delta x)]. \qquad (11.10)$$

The moment arm Δx can be eliminated from the above by considering the limit as it vanishes. In this limit ($\Delta x \to 0$), we have

$$f_{a,k}(t) = K_a c(t)\,[\psi_{k,x}(y_0) - \psi_{k,x}(y_1)]. \qquad (11.11)$$

Note that these forces enter the state equation as a term additive with the boundary layer vector $\underline{f}_t$. With multiple non-overlapping actuators, we have the superposition of the signals from the various actuators entering the plant; i.e.,

$$\underline{f}_a(t) = \sum_{m=1}^{M} \underline{f}_a^{(m)}(t), \tag{11.12}$$

where M is the number of actuators, and $\underline{f}_a^{(m)}(t)$ is the actuation vector (as above) for the m^{th} actuator.

The above equations give us a complete parametric model for the transfer between the beam motion and the sensor outputs, and between the control signals and the beam motion. The control algorithm is inserted between these sensor output signals and control input signals. Thus, from these equations, the control synthesis and simulation can proceed.

11.1.4 Supersonic Boundary Layers

A significant increase in complexity results from the assumption of a supersonic boundary layer. Here, the damping effects of the acoustic potential must be calculated in modal form, a task that requires a calculation on the order of Eq. 7.10 but with singular integrands.

11.1.5 Transitional Boundary Layers

Transitional flow can be modeled as a binary gating field that switches intermittently between the regimes of pure laminar and pure turbulent flow. In Phase I the binary field was modeled as being Markovian in time; follow-on investigations will require that this be extended to be Markovian in both time and space, which can be modeled as a dynamic Gibbs field. Transitional flow is expected to be a significant phenomenon only in subsonic flow regimes; in supersonic flow, the boundary layer is sufficiently well established so as not to be intermittent.

11.1.6 Multiple-Input, Multiple-Output Nonlinear Feedback Control

Digital signal processors (DSPs) can be used to control the panel based on adaptive polynomial neural network algorithms. In the Phase I effort, the modal control algorithms used might be characterized as "selfish," in that the controller for each mode was concerned only with minimizing the modal displacement of that mode. In

practice, however, effecting control of one mode will generally excite other modes, thereby causing spillover and increasing the displacement in these modes. It is desirable to have a more "selfless" control approach, one in which actuators work together as well as individually for the combined minimization of beam or panel modal displacement.

Although individual control loops could be constructed for each mode over which control is to be exercised, a single multivariate controller is more powerful than multiple univariate controllers, as cross-couplings between modes can be taken into consideration, as shown in Fig. 11.1; *this represents a perfectly general multi-input, multi-output controller (MIMO) for the panel vibration.* Note that there is *no* requirement that the number of force actuators be equal to the number of displacement sensors.

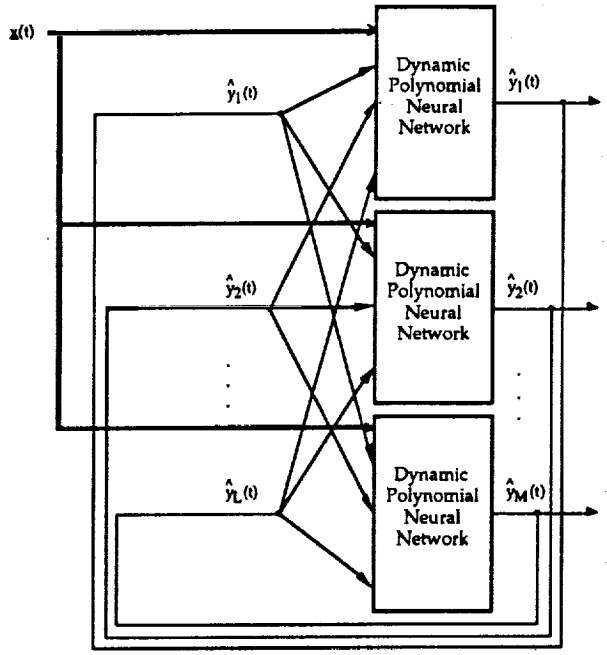

Figure 11.1: General Multi-Input, Multi-Output, Polynomial Neural Network (PNN) Mapping a Vector of L Sensor Measurements, $\underline{x}(t)$, into a Vector of M Controllers, $\underline{y}(t)$; Note that the Dynamic PNNs (see Fig. 9.2) may Contain Output Feedbacks and Internal Time Delays

Prior to the advent of neural networks, no general methods were available for the synthesis of MIMO, nonlinear, adaptive controllers. Neural networks may now be used to model implicitly the complex dynamic relationships and couplings between modes for completely general MIMO control. Recently [21], Barron Associates, Inc. (BAI) demonstrated that polynomial neural networks subsume Wiener-Volterra system identification techniques, which are often used for the identification of MIMO systems [20]; with PNNs, nonlinear and nonstationary (time-varying) systems, even those having infinite memory (e.g., oscillatory systems), may be readily identified. MIMO control represents an important research area having many potential applications.

BAI believes that successful development of such algorithms is feasible today. For the control of panel vibration, a MIMO polynomial neural network will be realized by adapting the network to achieve a globally optimum solution. This solution approach was not attempted in the Phase I effort due to time and budget limitations.

11.2 Laboratory Experiments

Laboratory experiments might be designed to simulate the turbulent boundary layer excitation and control of a section of an airplane panel consisting of a rectangular frame covered with a thin aluminum alloy skin. Three sets of experiments are suggested, beginning with applications of the control method to simple beam structures subject to controlled random loadings (e.g., random, progressive plane waves) and progressing to high velocity turbulent boundary layer excitation of panels.

11.2.1 Proof of Concept Experiments

The initial series of experiments are designed to demonstrate that a polynomial neural network can control the dynamic response of a simple, multimodal structure subject to random loadings. The structure will consist of a beam (clamped/clamped boundary conditions) mounted in one wall of an acoustic wave guide. The acoustic sources for the wave guide will consist of a series of horn drivers that generate plane, progressive waves with controlled amplitude and frequency spectra. The wave guide will be terminated anechoically to minimize end reflections. A series of sensors and actuators will be mounted along the outside surface of the beam in sufficient numbers to provide sensing and control in bandwidths containing high modal densities of the beam. It is suggested that approximately three sensor/actuator pairs should be used in this study.

Amplifiers for the actuators and signal conditioners for the sensors should be selected to be compatible with analog-to-digital (A/D) and digital-to-analog (D/A) computer control. The controller unit might consist of a digital signal processing (DSP) board interfaced with the A/D and D/A converters. For given excitation conditions, the controller unit drives the actuators independently, with a phase and magnitude prescribed by the neural network algorithm. Parameters to be varied in the demonstration experiment include the amplitude, bandwidth, and bandwidth center frequency of the progressive acoustic wave field. For this particular excitation, the controller unit will drive the actuators to minimize the mean square velocity of the beam response at a sufficient number of sensor locations to produce a global minimum.

11.2.2 Subsonic Turbulent Boundary Layer Excitation of a Uniform Beam

In this series of experiments, the acoustic wave guide is fitted with a centrifugal suction fan to provide turbulent boundary-layer excitation of beam modes up to flow velocities corresponding to Mach 0.1. Hot-wire measurements are taken in the turbulent boundary layer to determine the spectral content and spatial structure of the flow. A measure of success of the adaptive controller will be its ability to reduce the response of the beam globally as a function of flow velocity and turbulence level. As a further test of the robustness of the controller, turbulent bursts will be introduced artificially upstream of the beam to provide potentially destabilizing fluid dynamic forces.

For the experiments outlined in Sections 11.2.1 and 11.2.2, the controller strategy should be examined to determine its ability to control the response of a multimodal structure with high modal densities and subject to distributed loading based on stationary, as well as time-dependent, spectra. Additionally, as a major part of the above effort, the success of the control strategy as a function of the number of sensors and actuators should be investigated. Particular attention should be given to setting guidelines for the number of actuators and sensors required in the frequency band containing a specified number of structural modes.

11.2.3 High Velocity, Turbulent Boundary Layer Excitation of Panels

Following the successful completion of the above experiments, a third set of experiments should be conducted to control the vibration response of a rectangular plate subject to simulated, turbulent boundary layer excitations at high flow velocities. This excitation should simulate the distributed and random loading conditions of a high velocity, turbulent boundary layer. Based on the results of the

experiments outlined in Sections 11.2.1 and 11.2.2, the control algorithms should then be extended to accommodate a larger number of sensor/actuator elements. For the plate experiments, it is suggested that approximately 100 sensor/actuator pairs be involved, forming a ten by ten grid.

12 References

[1] D. W. Abbott and R. L. Barron, *Active Control of Complex Systems Via Neural Networks having Internal Feedback Paths and Time Delays*, Barron Associates, Inc., Technical Progress Report No. 1 for the Office of Naval Research, Contract N00014-89-C-0137, August 15, 1989.

[2] T. Bailey and J. E. Hubbard, "Distributed piezoelectric-polymer active vibration control of a cantilever beam," *J. Guid. Contr.*, 8(5), 605-611, 1985.

[3] G. K. Batchelor, *The Theory of Homogeneous Turbulence*. (Cambridge University Press: Cambridge, UK, 1960).

[4] A. R. Barron and R. L. Barron, "Statistical learning networks: A unifying view," *Computing Science and Statistics: Proceedings of the 20th Symposium on the Interface*, Reston, VA, April 1988, pp. 192-203.

[5] W. K. Blake, *Mechanics of Flow-induced Sound and Vibration*. (Academic Press: New York, 1986).

[6] S. E. Burke and J. E. Hubbard, Jr., "Distributed actuator control design for flexible beams," *Automatica*, **24**(5), 619-627, 1988.

[7] C.-Y. Chia, *Nonlinear Analysis of Plates*. (McGraw-Hill: New York, 1980).

[8] R. Courant and D. Hilbert, *Methods of Mathematical Physics - I*. (Interscience Publishers: New York, 1953).

[9] D. G. Crighton and J. E. Ffowcs Williams, "Real space-time Green's functions applied to plate vibration induced by turbulent flow," *J. Fluid Mech.*, **38**, 305-313, 1969.

[10] C.-K. Lee and F. C. Moon, "Modal sensors/actuators," *J. Appl. Mech.*, **112**, 434-441, 1990.

[11] F. C. DeMetz and M. J. Casarella, "An experimental study of the intermittent wall pressure bursts during natural transition of a laminar boundary layer," *Proc. AGARD- NATO Fluid Dynamics Panel*, Brussels (1973).

[12] J. S. DiStefano, A. R. Stubberud, and I. J. Williams, *Schaum's Outline of Theory and Problems of Feedback and Control Systems* (McGraw-Hill: New York, 1967).

[13] J. F. Elder, IV, R. L. Cellucci, and R. L. Barron, *Users' Manual: ASPN-II, Algorithm for Synthesis of Polynomial Networks*, Version 8.00, Barron Associates, Inc., July 1990.

[14] H. Kawai, "The piezoelectricity of poly(vinylidene) floride," *Jpn. J. Appl. Phys.*, **8**, 975-976, 1969.

[15] M. T. Landahl and E. Mollo-Christensen, *Turbulence and Random Processes in Fluid Mechanics*.. (Cambridge University Press: Cambridge, UK, 1986).

[16] M. Lesieur, *Turbulence in Fluids* (Martinus Nijhoff: Dordrecht, ND, 1987).

[17] L. Maestrello, "Design criterion of panel structure excited by turbulent boundary layer," *J. Aircraft*, **5**, 321-328, 1968.

[18] L. Maestrello, "Radiation from and panel response to a supersonic turbulent boundary layer," *J. Sound Vibr.*, **10**, 261-295, 1969.

[19] L. Maestrello, "Use of a turbulent model to calculate the vibration and radiation responses of a panel, with practical suggestions for reducing sound level," *J. Sound Vibr.*, **5**, 407-488, 1967.

[20] V. John Mathews, , "Adaptive polynomial filters," *IEEE Signal Processing Magazine*, July 1991, pp. 10-26.)

[21] B. E. Parker, Jr., R.L. Cellucci, and D.W. Abbott, *Active Control of Complex Processes via Dynamic Neural Networks: Combustion Processes in Propulsion Systems*, Barron Associates, Inc. Technical Progress Report No. 3 for the Office of Naval Research, Contract N00014-89-C-0137, April 1991.

[22] H. V. Poor, *An Introduction to Signal Detection and Estimation*. (Springer-Verlag: New York, 1988).

[23] G. M. Sessler, "Piezoelectricity in polyvinylidene flouride," *J. Acoust. Soc. Am.*, **70**, 1596-1608, 1981.

[24] F. T. Smith, "On transition to turbulence in boundary layers." In *Advances in Turbulence*, G. Comte-Bellot and J. Mathieu, Eds. (Springer-Verlag: Heidelberg, 1987), 27-36.

[25] D. H. Y. Yen, L. Maestrello and S. L. Padula, "Response of a panel to a supersonic turbulent boundary layer: Studies on a theoretical model," *J. Sound Vibr.*, **71**, 271-282, 1980.

Appendix A Derivation of Plant State Equations

The vector second-order ordinary differential equation for the damped beam is:

$$\left(\rho_1 \frac{d^2}{dt^2} + \gamma \frac{d}{dt} + D\Lambda\right) \underline{w}(t) = \underline{f}(t) + \underline{c}(t), \qquad (A.1)$$

where D is the plate rigidity; ρ_1 is the mass density (per unit area) of the panel; γ is the damping law; Λ is the the diagonal matrix with diagonal elements representing the eigenvalues of the solution to $\nabla^4\psi = \lambda\psi$; w is the modal displacement; and f and c are the vector boundary layer excitation and control forces, respectively.

Letting

$$x_1(t) = w_1(t),$$
$$x_2(t) = \dot{w}_1(t) = \dot{x}_1(t),$$
$$x_3(t) = w_2(t),$$
$$x_4(t) = \dot{w}_2(t) = \dot{x}_3(t),$$
etc.,

the state equations for this system can be written in the form

$$\dot{\underline{x}} = \mathbf{A}\,\underline{x} + \mathbf{B}\underline{f} + \mathbf{E}\underline{c} \qquad (A.2)$$

as

$$\begin{bmatrix} \dot{x}_1 \\ \dot{x}_2 \\ \dot{x}_3 \\ \dot{x}_4 \\ \cdot \\ \cdot \\ \cdot \\ \dot{x}_n \end{bmatrix} = \begin{bmatrix} 0 & 1 & 0 & 0 & \cdots & 0 \\ -D\lambda_1/\rho_1 & -\gamma/\rho_1 & 0 & 0 & \cdots & 0 \\ 0 & 0 & 0 & 1 & \cdots & 0 \\ 0 & 0 & -D\lambda_2/\rho_1 & -\gamma/\rho_1 & \cdots & 0 \\ \cdot & \cdot & \cdot & \cdot & \cdots & \cdot \\ \cdot & \cdot & \cdot & \cdot & \cdots & \cdot \\ 0 & 0 & 0 & 0 & -D\lambda_m/\rho_1 & -\gamma/\rho_1 \end{bmatrix} \begin{bmatrix} x_1 \\ x_2 \\ x_3 \\ x_4 \\ \cdot \\ \cdot \\ \cdot \\ x_n \end{bmatrix}$$

$$+\begin{bmatrix} 0 & 0 & 0 \\ 1/\rho_1 & 0 & 0 \\ 0 & 0 & 0 \\ 0 & 1/\rho_1 & 0 \\ \cdot & \cdot & \cdot \\ 0 & 0 & 0 \\ 0 & 0 & 1/\rho_1 \end{bmatrix}\begin{bmatrix} f_1 \\ f_2 \\ \cdot \\ \cdot \\ \cdot \\ f_m \end{bmatrix} + \begin{bmatrix} 0 & 0 & 0 \\ 1/\rho_1 & 0 & 0 \\ 0 & 0 & 0 \\ 0 & 1/\rho_1 & 0 \\ \cdot & \cdot & \cdot \\ 0 & 0 & 0 \\ 0 & 0 & 1/\rho_1 \end{bmatrix}\begin{bmatrix} c_1 \\ c_2 \\ \cdot \\ \cdot \\ \cdot \\ c_m \end{bmatrix} \qquad (A.3)$$

in which the A matrix is seen to be block diagonal with diagonal terms for the m^{th} mode of the form

$$\begin{bmatrix} 0 & 1 \\ -D\lambda_m/\rho_1 & -\gamma/\rho_1 \end{bmatrix} = \begin{bmatrix} 0 & 1 \\ -\omega_m^2 & -2\zeta_m\omega_m \end{bmatrix}.$$

To put this model into the form

$$x_{k+1} = \phi_k x_k + f_1 + c_1 \qquad (A.4)$$

for simulation requires the state transition matrix ϕ_k, which is defined by

$$\phi_k = \mathcal{L}^{-1}\left[(sI - A)^{-1}\right] t = \Delta \qquad (A.5)$$

where $\mathcal{L}$ is the Laplace operator, s is the complex frequency, Δ is the sampling interval, I is the identity matrix, and A is defined as above. For the m^{th} mode Eq. A.5 gives

$$\phi_k^m = \mathcal{L}^{-1}\begin{bmatrix} \dfrac{s + \gamma/\rho_1}{s^2 + \gamma s/\rho_1 + D\lambda_m/\rho_1} & \dfrac{1}{s^2 + \gamma s/\rho_1 + D\lambda_m/\rho_1} \\ \dfrac{-D\lambda_m/\rho_1}{s^2 + \gamma s/\rho_1 + D\lambda_m/\rho_1} & \dfrac{s}{s^2 + \gamma s/\rho_1 + D\lambda_m/\rho_1} \end{bmatrix}^{-1}_{t=\Delta} \qquad (A.6)$$

Comparing the polynomial in the denominator of each of the above terms with the characteristic second-order equation $s^2 + 2\zeta\,\omega_m s + \omega_m^2$, we see that $\gamma = 2\,\rho_1\,\zeta\,\omega_m$, where ζ is the damping ratio. The roots of the denominator polynomial are $-\alpha \pm j\omega_d$, where $\alpha = \zeta\omega_m$ is the damping coefficient of the m^{th} mode, $\omega_d = \omega_m\sqrt{1-\zeta^2}$ is the damped natural frequency of the m^{th} mode, and $\omega_m = \sqrt{D\lambda_m/\rho_1}$ is the undamped

natural frequency of the m^{th} mode. Note also that the time constant of the system is given by $\tau = 1/\alpha$ [12].

Damping of the beam is achieved, then, directly through the selection of ζ or indirectly through γ. Since $\alpha = \zeta\ \omega_m$, critical damping occurs when $\zeta = 1$ and $\alpha = \omega_m$. In [19], Maestrello defines a power law relationship $\alpha = 0.5\ \omega_d^{1/3}$ which, unless otherwise specified, is the damping coefficient used throughout this study.

Solving ϕ_k for the m^{th} mode gives

$$\phi_k^m = \begin{bmatrix} e^{-\alpha\Delta}[\gamma\ sin(\omega_d\Delta)/\rho_1 - \alpha\ sin(\omega_d\Delta) + \omega_d\ cos(\omega_d\Delta)]/\omega_d & e^{-\alpha\Delta} sin(\omega_d\Delta)/\omega_d \\ -\omega_m^2\ e^{-\alpha\Delta} sin(\omega_d\Delta)/\omega_d & e^{-\alpha\Delta}[cos(\omega_d\Delta) - \alpha\ sin(\omega_d\Delta)/\omega_d] \end{bmatrix}$$

(A.7)

Appendix B Modal Damping Ratio with Power-Law Proportionate Damping

In [19], Maestrello used a power-law proportional damping of the form

$$\gamma_m = \zeta_m \omega_m = 0.5\, \omega_d^{1/3} \qquad (B.1)$$

where, as discussed in Appendix A,

$$\omega_d = \omega_m \sqrt{1 - \zeta_m^2}\,, \qquad (B.2)$$

γ_m is the damping coefficient of the m^{th} mode, ω_m is the natural frequency of the m^{th} mode, and ζ_m is the damping ratio of the m^{th} mode. This is also the form of damping used in the computer simulations of Section 9. To determine the effective damping ratio, ζ_m, for each mode, Eqs. B.1 and B.2 may be combined to form the following equation:

$$\omega_d^2 + \frac{\omega_d^{2/3}}{4} = \omega_m^2\,. \qquad (B.3)$$

Substituting $x = \omega_d^{2/3}$ yields a cubic equation in x:

$$x^3 + \frac{x}{4} = \omega_m^2\,, \qquad (B.4)$$

which has one real and two complex roots. Table 9.1 gives the un

damped natural frequency of the first mode as ω_1 = 570.90 rad./sec. Substituting this value into Eq. B.4 and solving for the real root gives x = 68.818. Since

$$x = \omega_d^{2/3}, \qquad (B.5)$$

$$\sqrt{x} = \omega_d^{1/3}, \qquad \text{(B.6)}$$

and from Eq. B.1,

$$\zeta_1 = \frac{0.5\sqrt{x}}{\omega_1} = \frac{0.5\sqrt{68.818}}{570.90} = 0.007265. \qquad \text{(B.7)}$$

Similarly for mode two, the undamped natural frequency given in Table 9.1 is ω_2 = 1573.6 rad./sec., which gives a real root to Eq. B.4 of x = 135.29. Thus,

$$\zeta_2 = \frac{0.5\sqrt{x}}{\omega_2} = \frac{0.5\sqrt{135.29}}{1573.6} = 0.003696. \qquad \text{(B.8)}$$

REPORT DOCUMENTATION PAGE

Form Approved
OMB No. 0704-0188

1. AGENCY USE ONLY (Leave blank)	2. REPORT DATE	3. REPORT TYPE AND DATES COVERED
	December 1993	Contractor Report; January 16, 1991 - August 15, 1991

4. TITLE AND SUBTITLE
Adaptive Nonlinear Polynomial Neural Networks for Control of Boundary Layer/Structural Interaction

5. FUNDING NUMBERS
C NAS1-19271
WU 324-01-00

6. AUTHOR(S)
B. Eugene Parker, Jr., Richard L. Cellucci, Dean W. Abbott, Roger L. Barron, Paul R. Jordan III, and H. Vincent Poor

7. PERFORMING ORGANIZATION NAME(S) AND ADDRESS(ES)
Barron Associates, Inc.
Rt. 1, Box 159
Stanardsville, VA 22973-9511

8. PERFORMING ORGANIZATION REPORT NUMBER
SBIR-02.10-4400

9. SPONSORING/MONITORING AGENCY NAME(S) AND ADDRESS(ES)
National Aeronautics and Space Administration
Langley Research Center
Hampton, VA 23681-0001

10. SPONSORING/MONITORING AGENCY REPORT NUMBER
NASA CR-189645

11. SUPPLEMENTARY NOTES
Langley Technical Monitor: Richard J. Silcox
Final Report
SBIR Phase I

12a. DISTRIBUTION/AVAILABILITY STATEMENT
Unclassified–Unlimited

Subject Category 71

12b. DISTRIBUTION CODE

13. ABSTRACT (Maximum 200 words)

The acoustic pressures developed in a boundary layer can interact with an aircraft panel to induce significant vibration in the panel. Such vibration is undesirable due to the aerodynamic drag and structure-borne cabin noise that result. The overall objective of this work is to develop effective and practical feedback control strategies for actively reducing this flow-induced structural vibration.

This report describes the results of initial evaluations using polynomial neural network-based feedback control to reduce flow-induced vibration in aircraft panels due to turbulent boundary layer/structural interaction. Computer simulations are used to develop and analyze feedback control strategies to reduce vibration in a beam as a first step. The key differences between this work and that ongoing elsewhere in the active control of structural vibration are, firstly, that turbulent and transitional boundary layers represent broadband excitation and thus present a more complex stochastic control scenario than that of narrowband (e.g., laminar boundary layer) excitation; and secondly, that the proposed controller structures are adaptive nonlinear infinite impulse response (IIR) polynomial neural networks, as opposed to the traditional adaptive linear finite impulse response (FIR) filters used in most studies to date.

The controllers implemented in this study achieved vibration attenuation of 27 to 60 dB, depending on the type of boundary layer established by laminar, turbulent, and intermittent laminar-to-turbulent transitional flows. Application of multi-input, multi-output, adaptive, nonlinear feedback control of vibration in aircraft panels based on polynomial neural networks appears to be feasible today. Plans are outlined for Phase II of this study, which will include extending the theoretical investigation conducted in Phase I and verifying the results in a series of laboratory experiments involving both beam and plate models.

14. SUBJECT TERMS	15. NUMBER OF PAGES
Turbulent Boundary Layer/Structural Interaction; Structural Acoustics; Polynomial Neural Networks; Nonlinear Adaptive Feedback Control; Controlled Stochastic Partial Differential Equations	69
	16. PRICE CODE A03

17. SECURITY CLASSIFICATION OF REPORT	18. SECURITY CLASSIFICATION OF THIS PAGE	19. SECURITY CLASSIFICATION OF ABSTRACT	20. LIMITATION OF ABSTRACT
Unclassified	Unclassified	Unclassified	Unlimited